Is red blood cell a simple capsule?

V. Puthumana, Paul G. Chen, M. Leonetti, R. Lasserre, Marc Jaeger

To cite this version:

V. Puthumana, Paul G. Chen, M. Leonetti, R. Lasserre, Marc Jaeger. Is red blood cell a simple capsule?. 2022. ⟨hal-03795520⟩

HAL Id: hal-03795520
https://hal.science/hal-03795520v1

Preprint submitted on 6 Oct 2022

Banner appropriate to article type will appear here in typeset article

Is red blood cell a simple capsule?

V. Puthumana[1], P. G. Chen[1], M. Leonetti[2] †, , R. Lasserre[3] ‡, and M. Jaeger[1] ¶

[1]Aix Marseille Univ, CNRS, Centrale Marseille, M2P2, Turing Centre for Living Systems, France

[2]Aix Marseille Univ, CNRS, CINaM, Turing Centre for Living Systems, Marseille, France

[3]Aix Marseille Univ, INSERM, CNRS, CIML, Turing Centre for Living Systems, Marseille, France

(Received xx; revised xx; accepted xx)

Like other cells, the red blood cell membrane is composed of a lipid bilayer and a cytoskeleton, connected by protein junction complexes, with possible sliding. Despite this biological reality, it is most often modelled as a one-layer capsule or as a vesicle. An alternative is to consider a two-layers membrane, each mimicking either the lipid bilayer or the cytoskeleton. The in-plane elastic part brought by the cytoskeleton is modelled by a continuous constitutive law (capsule) or a discrete spring network. Considering four regimes representing the dynamics in shear flow, we computationally asses all the strategies with couplings such as capsule-capsule or capsule-network and vesicle-capsule or vesicle-network. The anisotropy artificially introduced by a discrete spring network is a source of numerical instability, especially for the coupling with a vesicle. Though the capsule-capsule and vesicle-capsule models show similarity in behaviour, considering fluidity and surface incompressibility when using a vesicle to represent the bilayer is not without consequences. Rigorous area conservation provides noticeable additional stiffness and fluidity allows lipid recirculation. Overall, our results suggest that modelling the membrane closer to the biological reality is more impactful than the largely debated issue about the stress-free shape for the cytoskeleton. Now, our results when comparing the capsule and the capsule-capsule models in tank-treading regime providentially highlight a new indicator of the right stress-free shape motivating new experimental investigations.

1. Introduction

The red blood cell (RBC) is a cell that during its maturation frees itself from all the usual internal organisation (Mohandas & Gallagher 2008; Kim *et al.* 2012). The richness of its mechanical behaviour therefore lies essentially in its membrane, which consists of a lipid bilayer (BL) supported by a cortical spectrin cytoskeleton (SC) (Evans & Skalak 2018; Mohandas & Evans 1994; Mohandas & Gallagher 2008; Kim *et al.* 2012). As a consequence, the numerical modelling of an RBC requires a good understanding of its organisation. It's why we start this introduction by recalling the main aspects, before coming to the aim of our study.

The BL consists mainly of four types of phospholipids, cholesterol and glycolipids

---

† Email address for correspondence: marc.leonetti@cnrs.fr
‡ Email address for correspondence: lasserre@ciml.univ-mrs.fr
¶ Email address for correspondence: marc.jaeger@centrale-marseille.fr

(Mohandas & Gallagher 2008). It also hosts a wide variety of proteins to ensure specific functions (Chien & Sung 1990; Mohandas & Evans 1994; Mohandas & Gallagher 2008; Lux 2016). It can be likened to a two-dimensional smectic crystal (Sackmann 1994). Thus, due to its fluid nature, it has no shear resistance (Evans & Hochmuth 1978; Evans & Skalak 2018). On the other hand, its expansion modulus ^ of the order of 450×10^{-3} N m^{-1} (Evans & Waugh 1977; Evans & Hochmuth 1978; Kim *et al.* 2012) gives it a quasi-incompressible property. An increase of only 3-4% of its area causes lysis of the cell (Mohandas & Gallagher 2008). This value is actually a representative of the entire RBC membrane, given the very small contribution of the SC. The BL also gives the entire membrane a very slight resistance to bending. Its very low bending modulus $_c$ of the order of 2×10^{-19} J (Evans & Hochmuth 1978; Mohandas & Evans 1994; Hwang & Waugh 1997; Scheffer *et al.* 2001) allows it to flicker by thermal agitation (Brochard & Lennon 1975; Peterson *et al.* 1992; Betz *et al.* 2009). However, in the absence of any other elastic contribution, it is the minimisation of the bending energy that determines its shape at rest (Canham 1970). The neutrality of the SC in this case could be explained by the existence of a remodelling process allowing the SC to relax its constraints (Nans *et al.* 2011). However, assuming that this remodelling is only active under certain conditions, notably deformation, the SC could just as well adopt a different reference shape than that imposed by the BL. In particular, a shape very close to the sphere has been proposed to explain the discrepancies in numerical modelling relative to a number of experimental results. In this hypothesis, a non-zero value of spontaneous curvature of the BL must be considered to recover the typical discocyte shape of the RBC at rest. Instead, a stomatocyte shape is obtained without this addition (Tsubota *et al.* 2014; Peng *et al.* 2014).

The traditional view of the SC is a network of spectrin filaments, mostly tetramers, forming a 2D net with a mostly hexagonal mesh. This SC coats the inner surface of the BL. A tetramer consists of two heterodimers of U-spectrin and V-spectrin, intertwined head to tail. Each of its two ends is connected to an actin junction complex (JC) (Sung & Vera 2003; Nans *et al.* 2011). However, more recent observations suggest greater complexity (Liu *et al.* 2003; Nans *et al.* 2011; Pan *et al.* 2018). Proteomic analysis (Bryk & Wiśniewski 2017; Gautier *et al.* 2018) indicate a density of proteins, including spectrin, that is two to three times greater than usually considered in models. This would increase the number of JCs from about 270 to over 700 JCs per $\mu\mathrm{m}^2$ (Feng *et al.* 2020). This leads to a much smaller estimate of the length of the spectrin filaments for a resting RBC. With a maximum length of the order of 200 nm and considering a non-linear behaviour law, the mechanical implication is obvious. Furthermore, this length deduced from the protein concentration and the assumption of a uniform distribution should only be considered as an average value. The observations show that the spectrin network is much more irregular, with inter-junctional distances varying from 20 nm to 97 nm (Nans *et al.* 2011), along with holes (Pan *et al.* 2018), hexamers and octamers to occur (Liu *et al.* 2003; Nans *et al.* 2011). The capacity for a passive or an active remodelling should also be considered (Nans *et al.* 2011). This SC provides the RBC membrane with the shear strength that the BL lacks. The measured shear modulus ` values vary from a few pN $\mu\mathrm{m}^{-1}$ to several hundred, depending on the intensity of the deformation specific to each measurement method (Feng *et al.* 2020). Beyond the measurement uncertainty, this large variation could be explained by the non-linear behaviour of spectrin filaments and the resulting hardening behaviour of the entire cytoskeleton (Feng *et al.* 2020).

The coupling of the SC with the BL is ensured by two types of JC, the actin JC already mentioned and the ankyrin JC. The latter provides a second attachment in the central region of each spectrin tetramer. They link to intrinsic BL proteins such as band-3 and glycophorins, which constitute the part of the JC located in the BL (Lux 2016). This part is bound to remain there, leading to a connection of an elastic nature in the direction perpendicular to the membrane. In contrast, the connection in the transverse directions is only ensured by the viscous friction of this part in the BL. The energy required to break the physical bonds involved in these JCs is sufficiently low that remodelling by metabolic or mechanical energy input can be considered (Gov & Safran 2005; Li *et al.* 2007).

The finest models are those carried out with Molecular Dynamics (MD). As the all-atom is too limited in time and space scales, the Coarse Graining (CGMD) version is used. In this case, the particles are represented by a group of several molecules (Li *et al.* 2007; Zhu *et al.* 2007; Li & Lykotrafitis 2012, 2014, 2015; Zhang *et al.* 2015). A state of the art is given in (Li *et al.* 2018*a*). In order to extend the numerical simulations to the RBC scale, this approach is even pushed to the limit of the Continuous Material Medium (CMM) (Li *et al.* 2018*a*). Each spectrin filament is simulated by a spring characterised by a polymer behaviour law like WLC (Discher *et al.* 1998; Li *et al.* 2005; Dao *et al.* 2006; Pivkin & Karniadakis 2008; Fedosov *et al.* 2010*a*,*b*; Peng *et al.* 2013; Pivkin *et al.* 2016). However, to reach the scale of a flowing RBC, the CG concept was eventually extended until the SC was represented by a network of only a few thousand or even a few hundred springs (Li *et al.* 2013, 2018*a*).

It is obvious that this process of increasing simplification is accompanied by a distancing from biomolecular reality. The modelling work therefore consists of identifying the dominant characteristics to be retained and how to consider them via more macroscopic behaviour laws. This concern is not only restricted to models inspired by MD. Considering the membrane of an RBC as a continuous surface medium, which is legitimate at the cell level (Evans & Hochmuth 1978), allows from the outset to free oneself from the molecular reality. The fact remains that the Fluid-Structure Interaction (FSI) problem represented by the behaviour of a flowing RBC, and given the observed complexity of this behaviour, requires a high degree of discretization. Studying a large population of these objects in hydrodynamic interaction therefore poses the same problem of identifying the modelling ingredients to be retained. It should be noted that the limit to which the concept of CG is pushed could make the distinction with CMM modelling less obvious and raises a question. Certainly, at the scale of tetramers, the SC is a discrete structure, representable by a network of springs. However, on the scale of the cell, given the high density of these filaments and the variability in their organisation, it appears rather as a continuous surface medium. In a CG logic, would it not be more legitimate to represent the SC by a continuous capsule-like surface medium than by a coarse network of a few thousand or a few hundred springs ?

More generally, disregarding any prejudice on the numerical method, it is legitimate to ask which modelling strategy at the cell scale would result from a reasoning based on the size criterion of the membrane constituents. In a CG logic, the most probable answer would be to retain at least the two most important structures, the SC and the BL. Enriching the model would then be to extend this high-pass filter in size downwards to distinguish constituents in each of these two main structures. However, this is by far not the most common approach. It has not been adopted because of the even greater need for simplification. In the CG approach, as in the CMM approach, it is a single surface structure model that is more systematically adopted.

In that strategy, mechanical properties of a macroscopic nature are necessarily sacrificed. Favouring the fluidity of the BL by a vesicle model does not allow to consider the membrane elasticity provided by the SC. Conversely, favouring the elasticity of the SC by a capsule model is at the expense of the fluid nature of the BL and only allows to consider approximately its surface incompressibility (Dodson & Dimitrakopoulos 2010). An exception is in 2D modelling where the vesicle model is the best compromise. Indeed, in 2D as well as in axial symmetry, neither the shear deformation mode nor the fluidity of the BL come in play. In any case, the possibility of sliding of the SC anchor points in the BL is completely forgotten.

The question is whether it really matters. The history of studies shows that relevant results have been obtained with all these approaches.

The absence of one property could be compensated by enhancing the action of another. Moreover, the dominant importance of the elastic properties of the SC has been shown in (Mendez & Abkarian 2018) for the case of pure shear flows and in (Hoore *et al.* 2018) for the RBC aggregation phenomenon. The capsule model is thus nowadays the preferred choice for a single layer modelling strategy of the RBC membrane. Considering only approximately the surface incompressibility constraint also offers a clear advantage in terms of the stiffness of the numerical problem. The answer to the question may therefore be negative, if the aim is to reproduce the experimental observations qualitatively. The answer may also be negative for studies of blood rheology, if the second-order phenomena involved do not fundamentally modify the collective effects. However, evidence is accumulating that the dynamics of RBCs are very sensitive to second-order parameters such as the reference shape of the SC (Zarda *et al.* 1977; Fischer *et al.* 1981; Lim *et al.* 2002; Fischer 2004; Dupire *et al.* 2012; Peng *et al.* 2014; Tsubota *et al.* 2014; Viallat & Abkarian 2014; Sinha & Graham 2015; Peng *et al.* 2015*b*). It is therefore not easy to draw conclusions. On the other hand, giving a negative answer is less obvious if the objective is to identify the share of each component in a macroscopic behaviour, in particular with a view to understanding pathologies.

Although largely less represented than the capsule model, models that distinguish the SC from the BL also exist (Peng *et al.* 2015*a*; Li *et al.* 2018*b*), both in the CG spring network approach (Noguchi & Gompper 2005; McWhirter *et al.* 2011; Peng *et al.* 2013; Li *et al.* 2014; Pivkin *et al.* 2016; Chang *et al.* 2016, 2017) and in the CMM thin-shell approach (Peng *et al.* 2010, 2011, 2014, 2015*b*; Salehyar & Zhu 2016; Zhu *et al.* 2017; Lu & Peng 2019). In the following we will refer to them as two-layer composite models or simply BL-SC composite models or composite models. The studies carried out with these models have provided arguments in their favour (Zhang *et al.* 2015; Peng *et al.* 2015*a*; Li *et al.* 2018*b*). However, to our knowledge, no study has really compared the two strategies quantitatively. The only evidence that can be given is that the second strategy corresponds better to biological reality.

In (Lyu *et al.* 2018) we have shown that in the CMM approach, the kinematics of the SC and the BL can be differentiated without having to duplicate the meshes. The same possibility seems to be excluded for a CG model since one has to choose between bond-flipping or not (Kroll & Gompper 1992). In CMM, the distinction between fluid and solid is more about the formulation of the conservation equations, in Lagrangian variables for the solid and Eulerian for the fluid. Lagrangian kinematics for the SC (solid) and Eulerian kinematics for the BL (fluid) can thus be implemented with a single mesh. Obviously, the consideration of a different kinematics in the direction normal to the membrane is not possible. However, this only prohibits studies involving detachment of the SC from the BL.

The numerical simulation platform we have developed implements the Boundary Integrals Method (BIM) (Pozrikidis 1992) by finite elements (BEM) (Pozrikidis 2002). Both the membrane and the ambient media are seen as continuous material media. The BEM implementation is based on Isogeometric Analysis (IGA) (Cottrell *et al.* 2009). The numerical representation of the geometry, as well as of all the physical fields involved, is obtained by Loop's subdivision (Loop 1987; Cirak *et al.* 2000; Cirak & Ortiz 2001). Called SOFT, this platform allows to study an FSI problem in Stokes flow for a variety of deformable micro-objects, surfactant coated drop, vesicle and capsule (Boedec *et al.* 2017), and even to combine them. This opens up the possibility of comparing different options for RBC modelling, with equal accuracy in all other aspects. The comparison can therefore be truly quantitative. The aim of this study is the comparison of the capsule (C) model with models that distinguish the SC from the BL by a combination of capsule-capsule (C-C) and vesicle-capsule (V-C), as well as capsule-spring (C-S) and vesicle-spring (V-S). The vesicle (V) model is also considered for flow configurations that allow it.

The question seemed relevant for another reason. It concerns an aspect that has been relatively ignored until now, but which is beginning to enter the debate : surface viscosity (Fedosov *et al.* 2014; Li *et al.* 2013; Vlahovska *et al.* 2013; Yazdani & Bagchi 2013; Freund 2014; Gounley & Peng 2015; Peng *et al.* 2015*a*; Prado *et al.* 2015; Li *et al.* 2018*b*; Guglietta *et al.* 2020; Tsubota 2021). Whether the kinematics of the SC and BL should be distinguished is a legitimate question. It is sufficient to consider the source of dissipation represented by the friction of the JCs in the BL. More generally, identifying the physical mechanisms that cause dissipation seems to be difficult if we reason only in terms of effective viscosity. The great disparity of the measured values of surface viscosity of the RBC is a proof of this. However, we reserve the study of this aspect for a future paper, restricting ourselves here to the elastic behaviour.

The modelling strategies we propose to compare are presented first, following by a comparative study. Finally, we discuss the results and conclude with the main lessons learned.

2. RBC modelling strategies

The vesicle and capsule models implemented in SOFT are described in (Boedec *et al.* 2017) and in (Lyu *et al.* 2021) for the application to confined spaces. The V model considers the fluid nature of the membrane, with a rigorous treatment of the surface incompressibility constraint by projection of the 3D velocity field into a space with zero surface divergence. Moreover, the iso-parametric description of the geometry allows (thanks to its regularity at least ^{1} and even ^{2} almost everywhere) to consider the Helfrich bending energy in a rigorous mathematical weak formulation. The C model can consider several models of polymerised membrane behaviour. It can also incorporate bending elasticity, via the Helfrich formulation developed for the V model or via other more common forms of thin-shell modelling. The contribution of a shear and expansion surface viscosity developed initially for a drop with surfactant (Gounley *et al.* 2016) is also available for the V and C models. However, this option will not be used here. Since the description of these basic models can be found elsewhere (Boedec *et al.* 2017; Lyu *et al.* 2021), we can focus on the coupling strategy. It is inspired by BL-SC composite models developed by others.

In the context of CGMD approaches, the jump to a CG representation of the cytoskeleton by a network of springs is generally attributed to Discher, Boeal and Boey (Discher *et al.* 1998; Li *et al.* 2018*a*). In contrast, the idea of modelling the RBC membrane as two connected surface material media was first proposed in the CMM framework by Krishnaswamy (Krishnaswamy 1996). However, the formulation remained at the theoretical stage. A trace of the idea is present in the CG model of Noguchi and Gompper (Noguchi & Gompper 2005; McWhirter *et al.* 2011), with two spring networks that use the same nodes and therefore are forced to move together. The only difference concernes the network of springs that represents the BL. Its fluid nature is simulated by the bond-flipping method, previously developed to study vesicles (Kroll & Gompper 1992). The idea has been much more widely developed by Peng and Zhu and colleagues in the form of a three levels model (Peng *et al.* 2015*a*; Li *et al.* 2018*b*). The first two levels (I and II) are molecular. They allow estimates of the macroscopic elastic properties of the SC to be made up to the last level, the cell level (level III). For this level, a CMM approach using shell finite elements is used, both for the SC and the BL in (Peng *et al.* 2010, 2011; Peng & Zhu 2013; Peng *et al.* 2014) and more recently in (Salehyar & Zhu 2016; Zhu *et al.* 2017) and in (Lu & Peng 2019). Each of these two structures has its own mesh, with the possibility of different movement of the nodes of one mesh relative to the other. The relative tangential motion is driven by the frictional forces of the anchoring

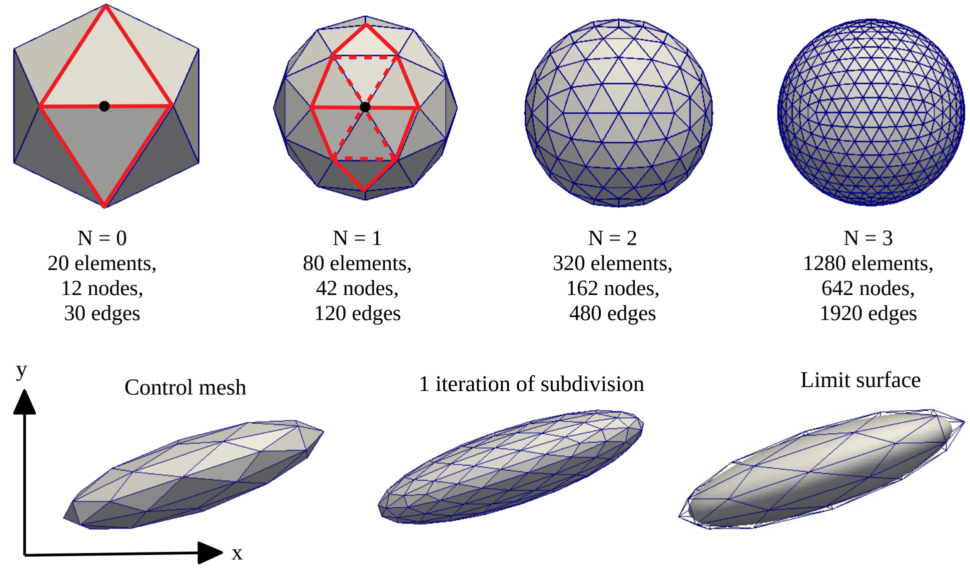

N = 0
20 elements,
12 nodes,
30 edges

N = 1
80 elements,
42 nodes,
120 edges

N = 2
320 elements,
162 nodes,
480 edges

N = 3
1280 elements,
642 nodes,
1920 edges

FIGURE 1 – Principle of mesh refinement by Loop's subdivision, starting from the icosahedron (top) and principle of zero error geometry discretisation in IGA (bottom). Following Loop's subdivision rules, whatever the level of refinement, the same limit surface is represented.

proteins of the SC in the BL. Relative motion in the normal direction is formulated as a contact problem between two surfaces. Surprisingly, both structures use a solid shell model, i.e. a capsule. The difference is simply that the bending rigidity is ignored for the SC and a very low shear modulus is used for the BL. In addition, a large expansion modulus is used for the latter, to approximate surface incompressibility (Zhu *et al.* 2017). In (Peng *et al.* 2013; Li *et al.* 2014; Pivkin *et al.* 2016; Chang *et al.* 2016, 2017) this level III model is implemented in the CG approach with the DPD method. The two structures are represented by two spring networks. It is specified in (Chang *et al.* 2017) that the diffusion of lipid molecules is not considered. This suggests that the BL fluidity is also ignored in this CG variant. Finally, in (Chang *et al.* 2016, 2017), Level I and II models are replaced by the CGMD model of (Li & Lykotrafitis 2012).

In (Lyu *et al.* 2018) we have been inspired by this work to show the feasibility of coupling the V model with a network of springs materialized by the edges of the mesh elements. In this coupling option, the elastic forces induced by the deformation of the SC are expressed at the nodes of the mesh, as a function of the elongation of the edges that connect them. This elongation is defined relative to their length for a reference shape of the SC, to be specified. An elastic force resultant is obtained at each node by summation over all the edges that connect it to its direct neighbours. These elastic forces are transmitted to the BL via the forces induced by the friction of the JCs in the BL, with which they balance.

The usual approach of meshing in SOFT is to start with the icosahedron, as shown in figure 1. An initial uniform mesh is obtained by a number $\#$ of subdivisions of it. The value $\# = 0$ simply corresponds to the starting icosahedron. Each of its twenty triangular faces corresponds to a single Loop element, i.e. $\#_{elem} = 20$ equilateral triangular elements, $\#_{node} = 12$ nodes and $\#_{edge} = 30$ edges. With each refinement of the mesh by a subdivision level, each element is subdivided into four equivalent equilateral elements, with a node inserted at the centre of each edge. The spatial position of all nodes in this refined mesh is determined by Loop's rules to ensure zero geometric representation error. The level $\# = 1$

leads to ($\#_{elem} = 80$- $\#_{node} = 42$- $\#_{edge} = 120$) and $\# = 2$ to ($\#_{elem} = 320$- $\#_{node} = 162$- $\#_{edge} = 480$). Satisfactory accuracy can usually be achieved with $\# = 3$, thus ($\#_{elem} = 1280$- $\#_{node} = 642$- $\#_{edge} = 1920$). Note that the twelve nodes of the $\# = 0$ level have a fifth-order connectivity, unlike all the other nodes introduced afterwards, which have a sixth-order connectivity. These twelve nodes, an inevitable trace of the icosahedron, are called singular. The regularity of the Loop approximation is only ^{1} there, while it is ^{2} everywhere else.

The velocity field of the fluid film flow corresponding to the BL is the surface trace of the 3D ambient bulk fluid flow. The latter is obtained by BEM with the surface mesh just described. Thus, the velocity of the lipid medium is known at each node and can be determined at any point of an element via Loop's interpolation functions. The normal component of this velocity field allows the shape of the RBC to evolve between two time steps of the numerical simulation. On the other hand, the updating of the position of the nodes tangentially to the membrane is identified with the kinematics of the SC. The normal component of the velocity characterising this kinematics coincides with that of the BL. The tangential component is determined by the principle of equilibrium of the elastic forces exerted by the SC with the viscous friction forces of the points of attachment of the latter in the BL. The latter are proportional to the velocity difference between the two kinematics. Restricting the presentation to the unconfined case for simplicity and in the absence of viscosity contrast, the set can be formulated as follows (Lyu *et al.* 2018)

$$\boldsymbol{v}^{BL} = \mathbf{P}\left(\boldsymbol{v}^{\infty} + \mathbf{G}\boldsymbol{f}^{RBC}\right) \quad \text{with} \quad \boldsymbol{f}^{RBC} = \boldsymbol{f}^{BL} + \boldsymbol{f}^{SC} \tag{2.1}$$

$$\boldsymbol{x}(C + 3C) = \boldsymbol{x}(C) + 3C\boldsymbol{v}^{SC} \tag{2.2}$$

The position field of the points on the mesh surface is denoted by $\boldsymbol{x}$. The velocity fields are denoted by $\boldsymbol{v}$, with superscripts BL for the bilayer and SC for the cytoskeleton, while ∞ denotes the imposed background flow. The Green's operator associated with the Stokeslet is denoted by $\mathbf{G}$. The projection operator on a subspace with zero surface divergence is denoted by $\mathbf{P}$. It ensures that the surface tension W, Lagrange multiplier of the surface incompressibility constraint, is such that the surface divergence of the velocity field $\boldsymbol{v}^{BL}$ is zero. The surface densities of force induced by the BL and SC correspond to $\boldsymbol{f}^{BL}$ and $\boldsymbol{f}^{SC}$, respectively. Their sum $\boldsymbol{f}^{RBC} = \boldsymbol{f}^{BL} + \boldsymbol{f}^{SC}$ corresponds to the surface force density exerted by the entire RBC membrane on the ambient fluids.

The matrix expression of the system (2.1)-(2.2), as well as the principle of the solution algorithms, are given in (Boedec *et al.* 2017; Lyu *et al.* 2018, 2021). We invite the interested reader to refer to it, pointing out that the rest of the paper is accessible without it. On this basis, which has been validated in our studies of vesicle and capsule objects, several strategies for RBC modelling are possible.

2.1. *Single layer vesicle model (V)*

The vesicle model is retrieved with $\boldsymbol{f}^{SC} = 0$ and

$$\boldsymbol{f}^{BL}(\boldsymbol{x}) = \boldsymbol{f}^{\gamma}(\boldsymbol{x}) + \boldsymbol{f}^{e\perp}(\boldsymbol{x}) = -\frac{X ,^{BL}}{X\boldsymbol{x}} = -\frac{X(,^{\gamma} + ,^{H})}{X\boldsymbol{x}} \tag{2.3}$$

$$,^{\gamma} = \int_S W\mathrm{d}(\quad - \quad ,^{H} = \int_S F_S^H\mathrm{d}(\quad - \quad F_S^H = \frac{c}{2}(2 \quad + 2_0)^2 \tag{2.4}$$

The $\boldsymbol{f}^{e\perp}$ contribution corresponds to the out-of-plane elastic forces, i.e. the bending forces induced by the Helfrich surface energy density F_S^H. It involves the mean curvature and the spontaneous curvature 2_0. The latter is defined by $2_0 = -2 \;\; _0$, where $_0$ is the mean curvature of the spontaneous or reference shape of the membrane. For zero spontaneous curvature, we obtain the very simple expression $F_S^H = 2 \ \ _c \ \ ^2$. The contribution of the Gaussian curvature, which in principle occurs in F_S^H, has been omitted. It is not useful by virtue of the Gauss-Bonnet theorem since we are not considering a change in surface topology. The contribution of $\boldsymbol{f}^\gamma$ corresponds to the forces induced by the surface tension. It is an out-of-plane force contribution for a constant tension but also in-plane if the tension varies since $\boldsymbol{f}^\gamma = 2W \ \ \boldsymbol{n} + \nabla_s W$.

2.2. *Single layer capsule model (C)*

The capsule model with Helfrich bending energy is found by replacing the projector **P** by the identity, with $\boldsymbol{f}^{SC} = 0$ and

$$\boldsymbol{f}^{BL}(\boldsymbol{x}) = \boldsymbol{f}^{e||}(\boldsymbol{x}) + \boldsymbol{f}^{e\perp}(\boldsymbol{x}) = -\frac{X\,,\ ^{BL}}{X\boldsymbol{x}} = -\frac{X(\,,\ ^{SK} + \,,\ ^{H})}{X\boldsymbol{x}} \tag{2.5}$$

$$,\ ^{SK} = \int_{S^0} F_{S^0}^{SK}\,\mathrm{d}(^0 \quad - \quad F_{S^0}^{SK} = \ _s(\ _1^2 + 2 \ _1 - 2 \ _2 + \ ^{SK} \ _2^2) \tag{2.6}$$

The $\boldsymbol{f}^{e||}$ contribution corresponds to the stresses deduced from a polymerized membrane strain energy, usually defined on the reference configuration.The expression typically used to model the strain hardening behaviour of the RBC membrane is that of Skalak $F_{S^0}^{SK}$ (Skalak *et al.* 1973). The surface shear stiffness ` corresponds to $\ _S$. The area variations are controlled by the coefficient $\ ^{SK}$. Indeed, the second invariant of the surface deformation tensor $\ _2 = \__1^2 \__2^2 - 1$ must cancel for an incompressible surface. This limiting case is obtained by making $\ ^{SK}$ tend to infinity. In practice, the numerical problem becomes too steep when we exceed a hundred. The addition of a global conservation constraint of the surface is then necessary to avoid a too strong drift of the surface area. The first invariant corresponds to $\ _1 = \__1^2 + \__2^2 - 2$. In these two invariants, $\__1$ and $\__2$ represent the main strains. The contribution of $\boldsymbol{f}^{e\perp}$ corresponds to the bending out of plan elastic forces. It is deduced from the Helfrich surface energy density F_S^H, as for the vesicle model.

2.3. *BL-SC composite vesicle-capsule model (V-C)*

The composite V-C model is obtained by using the expression (2.3) of $\boldsymbol{f}^{BL}$ of the V model and with

$$\boldsymbol{f}^{SC}(\boldsymbol{x}) = \boldsymbol{f}^{e||}(\boldsymbol{x}) = -\frac{X\,,\ ^{SC}}{X\boldsymbol{x}} = -\frac{X\,,\ ^{SK}}{X\boldsymbol{x}} \tag{2.7}$$

The incompressibility constraint is ensured rigorously as for the V model by the action of the **P** projector. The coefficient $\ ^{SK}$ of Skalak's law can then be freely fixed to represent only the contribution of the SC. Of course, this contribution is negligible compared to the resistance to expansion provided by the BL. The SC therefore only contributes effectively by providing its resistance to shear deformation.

2.4. *BL-SC composite capsule-capsule model (C-C)*

The composite C-C model is obtained by using the expression (2.5) of $\boldsymbol{f}^{BL}$ of the C model and the expression (2.7) of $\boldsymbol{f}^{SC}$ of the V-C model. The modelling of the SC is therefore the same as in the V-C model. On the other hand, the contribution $\boldsymbol{f}^{e||}$ which intervenes in $\boldsymbol{f}^{BL}$ should allow the fluid behaviour of the BL to be approached via a capsule model. The elastic shear modulus $\ _S$ must therefore be chosen to be sufficiently small that the contribution to the shear strength is negligible compared to that of the SC. The projector **P** being taken equal to the identity, the surface incompressibility stress is approximated as in the capsule model by fixing the coefficient ^{SK} of Skalak's law as large as possible and avoiding too much surface area drift through an overall conservation constraint.

2.5. *BL-SC composite vesicle-spring model (V-S) and capsule-spring model (C-S)*

The composite V-S and C-S models are obtained by replacing the capsule model to simulate the SC by a network of springs materialized by the edges of the mesh. The elastic force field $\boldsymbol{f}^{SC}(\mathbf{x})$ induced by the SC then takes a discrete form with a resultant at each node of the mesh. This can be translated by introducing the Dirac function $\boldsymbol{x}_n$ which is non-zero only at the node of position $\boldsymbol{x}_n$

$$\boldsymbol{f}^{SC}(\boldsymbol{x}) = \sum_{n=1}^{N_{node}} \boldsymbol{F}_n^{SC} X_{\boldsymbol{x}_n}(\boldsymbol{x}) \quad - \quad \boldsymbol{F}_n^{SC} = \sum_p \boldsymbol{F}_{np}^{SC} = \sum_p \quad {}_{np}(\boldsymbol{x}_p - \boldsymbol{x}_n) \tag{2.8}$$

The sum concerns all nodes ? connected to node = by an edge =? of the mesh. This edge materializes one of the springs of the network. Its mechanical behaviour is characterised by the spring stiffness coefficient $\quad_{np}$. As in (Lyu *et al.* 2018), we use the non-linear FENE-POW behaviour law

$$\boldsymbol{F}_n^{SC} = -\frac{X \, , \, ^{SC}}{X\boldsymbol{x}_n} \quad - \quad , \, ^{SC} = \frac{1}{2}\sum_{n=1}^{N_{node}} \sum_p \, ,_{np} \tag{2.9}$$

$$,_{np} = -\frac{:_a}{2}(;_{np}^{max})^2 \log(1 - \mathtt{G}_{np}^2) + \frac{:_r}{(U-1);_{np}^{\alpha-1}} \tag{2.10}$$

The length of the spring =? is $;_{np} = \|\boldsymbol{x}_p - \boldsymbol{x}_n\|$, with $;_{np}^{max}$ its maximum extension and $\mathtt{G}_{np} = ;_{np}/;_{np}^{max}$ their ratio. The first contribution is an attraction potential driven by the coefficient $:_a$. The second is a repulsion potential regulated by the coefficients $:_r$ and U. After adjustment to the reference configuration and the targeted effective shear modulus `, the stiffness coefficient $\quad_{np}$ is finally expressed as

$$_{np} = \frac{4\,`}{\sqrt{3}\left(\frac{2x_0^2}{1-x_0^2} + U + 1\right)}\left(\frac{1-\mathtt{G}_0^2}{1-\mathtt{G}_{np}^2} - \frac{\mathtt{G}_0^{\alpha+1}}{\mathtt{G}_{np}^{\alpha+1}}\right) \tag{2.11}$$

As in (Lyu *et al.* 2018), $\mathtt{G}_{np}^0 = \mathtt{G}_0 = 1/2 \bullet 05$ and $U = 2$.

2.6. *Elastic forces determination*

For all composite models, the coupling between the BL and the SC is provided by the friction of the JCs in the BL. Let $\boldsymbol{f}^{BL/SC}$ be the surface density of frictional force exerted by the BL on the SC. So, by the action-reaction principle, $\boldsymbol{f}^{SC/BL} = -\boldsymbol{f}^{BL/SC}$ is the surface density of frictional force exerted by the SC on the BL. Note that for a spring network, the discrete form $\boldsymbol{f}^{BL/SC} = \sum \boldsymbol{F}_n^{BL/SC} X\boldsymbol{x}_n$ has to be used. The static equilibrium for each of the two structures gives

$$\boldsymbol{f}^{SC} + \boldsymbol{f}^{BL/SC} = 0 \quad - \quad \boldsymbol{f}^{BL} + \boldsymbol{f}^{SC/BL} + \boldsymbol{f}^{ext} = 0 \tag{2.12}$$

The sum of the two equations shows that the action of the ambient fluids on the RBC membrane is in equilibrium with the forces induced by the deformation of the RBC, as it should be for FSI in the Stokes regime

$$\boldsymbol{f}^{ext} = -\boldsymbol{f}^{RBC} = -(\boldsymbol{f}^{BL} + \boldsymbol{f}^{SC}) \tag{2.13}$$

In SOFT, the structural forces are determined as usual with the finite element method by a weak formulation, via the virtual work principle

$$X\,,^{ext} + X\,,^{int} = 0 \tag{2.14}$$

with

$$X\,,^{ext} = \int_S \boldsymbol{f}^{ext}\cdot X\boldsymbol{x}\;\mathrm{d}(= -\int_S \boldsymbol{f}^{RBC}\cdot X\boldsymbol{x}\;\mathrm{d}(\tag{2.15}$$

$$\begin{aligned} X\,,^{int} &= -(X\,,^{BL} + X\,,^{SC}) \qquad (2.16)\\ &= \int_S -\frac{X\,,^{BL}}{X\boldsymbol{x}}\cdot X\boldsymbol{x}\;\mathrm{d}(+ \int_S -\frac{X\,,^{SC}}{X\boldsymbol{x}}\cdot X\boldsymbol{x}\;\mathrm{d}(\\ &= \int_S \boldsymbol{f}^{BL}\cdot X\boldsymbol{x}\;\mathrm{d}(+ \int_S \boldsymbol{f}^{SC}\cdot X\boldsymbol{x}\;\mathrm{d}(\end{aligned}$$

For a capsule or vesicle with a membrane modelled in CMM, the virtual work of the internal forces can be written as a function of the surface stress and strain tensors

$$\begin{aligned} X\,,^{int} &= -\int_S \left[f^{\alpha\beta} X(\ \ _{\alpha\beta}) + `^{\alpha\beta} X(\ \ _{\alpha\beta})\right] \mathrm{d}( \\ &= \int_S \left[ \frac{1}{2} f^{\alpha\beta} X(0_{\alpha\beta}) + `^{\alpha\beta} X(1_{\alpha\beta})\right] \mathrm{d}(\qquad (2.17) \end{aligned}$$

The tensor of components $\ \ _{\alpha\beta} = \left(0_{\alpha\beta} - 0^0_{\alpha\beta}\right)/2$ is the surface Green-lagrange strain tensor. The tensor of components $\ \ _{\alpha\beta} = \left(1_{\alpha\beta} - 1^0_{\alpha\beta}\right)$ is a measure of bending strain. The $0_{\alpha\beta}$ are the components of the metric tensor. Its determinant $0 = 34C(\mathbf{a})$ allows us to express the surface element as a function of the surface parameterisation $(B^1\text{-}B^2)$ as $\mathrm{d}(= \sqrt{0}\;\mathrm{d}B^1\mathrm{d}B^2$. The tensors of components $f_{\alpha\beta}$ and $`_{\alpha\beta}$ correspond to the stresses induced by the membrane and bending strains.

For a capsule modelled as a network of springs, we have more simply

$$X\,,^{int} = \sum_{n=1}^{N_{node}} \boldsymbol{F}_n^{SC}\cdot X\boldsymbol{x}_n = \sum_{n=1}^{N_{node}}\sum_{p}\ \ _{np}(\boldsymbol{x}_p - \boldsymbol{x}_n)\cdot X\boldsymbol{x}_n \tag{2.18}$$

It is therefore only necessary to add these point forces at each node of the mesh.

2.7. *Drag forces determination*

Let us denote by $\ \ _{f_{JC}}$ the mean friction coefficient of a JC in the BL. On average, the frictional force generated by the movement of a JC in the BL is written

$$\begin{aligned} \boldsymbol{F}_{JC}^{BL/SC} &= \ \ _{f_{JC}}\left(\boldsymbol{v}^{BL}(\boldsymbol{x}_{JC}) - \boldsymbol{v}^{SC}(\boldsymbol{x}_{JC})\right) \\ &= \ \ _{f_{JC}}\boldsymbol{v}^{BL/SC}(\boldsymbol{x}_{JC}) = -\ \ _{f_{JC}}\boldsymbol{v}^{SC/BL}(\boldsymbol{x}_{JC}) \qquad (2.19) \end{aligned}$$

The equivalent friction coefficient per unit area of membrane $\ \ _f$ is defined by

$$\int_{\triangle S} \ \ _f\,\boldsymbol{v}^{BL/SC}(\boldsymbol{x})\mathrm{d}(= \sum_{\boldsymbol{x}_{JC}\in\triangle S} \ \ _{f_{JC}}\boldsymbol{v}^{BL/SC}(\boldsymbol{x}_{JC}) \tag{2.20}$$

For a patch of surface $\triangle($ sufficiently small that the variations of speed can be neglected (i.e. $\forall\boldsymbol{x}\in\triangle(\text{-}\boldsymbol{v}^{BL/SC}(\boldsymbol{x}) = \boldsymbol{v}^{BL/SC}(\boldsymbol{x}_{JC}) \approx \mathrm{cst}$), we obtain

$$\ \ _f\,\triangle(= \ \ _{f_{JC}}\#_{JC} \tag{2.21}$$

or, by introducing the areal density of JC

$$f = \frac{\#_{JC}}{\triangle (} \quad f_{JC} = d_{JC} \quad f_{JC} \tag{2.22}$$

We consider the surface density d_{JC} to be constant but the following extension is of course possible

$$f\,(\boldsymbol{x}) = d_{JC}(\boldsymbol{x}) \quad f_{JC} \tag{2.23}$$

It allows to consider a variable density of JC in the RBC membrane, as experimentally observed (Nans *et al.* 2011). Moreover, by adding the time dependence and by means of an evolution law, it also makes it possible to consider a remodelling of the SC.

The equivalent friction coefficient per node f_n to be used in a spring network model of the SC is defined by

$$f_n \boldsymbol{v}^{BL/SC}(\boldsymbol{x}_n) = \int_{\triangle S_n} d_{JC} \quad f_{JC} \; \boldsymbol{v}^{BL/SC}(\boldsymbol{x})\mathrm{d}(\tag{2.24}$$

where $\triangle (_n$ is the portion of the surface associated with node =. It is assumed to be small enough that velocity variations can be neglected.

Hence the expression of f_n as a function of f_{JC} and f

$$f_n = \triangle (_n \, d_{JC} \quad f_{JC} = \triangle (_n \quad f \tag{2.25}$$

2.8. *Kinematics of the SC*

In a CMM formulation of the SC, at any point on the surface representing it, the velocity of the SC relative to the BL is given by

$$\boldsymbol{v}^{SC/BL}(\boldsymbol{x}) = \boldsymbol{v}^{SC}(\boldsymbol{x}) - \boldsymbol{v}^{BL}(\boldsymbol{x}) = -\frac{1}{f}\boldsymbol{f}^{BL/SC}(\boldsymbol{x}) = \frac{1}{f}\boldsymbol{f}^{SC}(\boldsymbol{x}) \tag{2.26}$$

Using the weighted residual method with the test functions equal to $X\mathbf{x}$, we derive the weak formulation

$$\int_S \boldsymbol{v}^{SC/BL}(\boldsymbol{x})\cdot X\boldsymbol{x}\,\mathrm{d}(= \frac{1}{f}\int_S \boldsymbol{f}^{SC}(\boldsymbol{x})\cdot X\boldsymbol{x}\,\mathrm{d}(= -\frac{1}{f} X\,, \;^{SC} \tag{2.27}$$

The second member of the corresponding system is already constructed in the context of the determination of the elastic membrane forces of the RBC. The first member is simply expressed as a function of the mass matrix whose expression in terms of the Loop interpolation functions is given in (Boedec *et al.* 2017).

In a spring network model of the SC, the tangential velocity of each node is more simply given by

$$\boldsymbol{v}^{SC/BL}(\boldsymbol{x}_n) = \boldsymbol{v}^{SC}(\boldsymbol{x}_n) - \boldsymbol{v}^{BL}(\boldsymbol{x}_n) = \frac{1}{f_n}\boldsymbol{F}_n^{SC} \tag{2.28}$$

3. Comparison of RBC modelling strategies on shear flow

The simple shear flow is certainly the configuration that has been most considered to characterise the mechanics of a flowing RBC. By choosing to orient the reference frame so that the G axis corresponds to the direction of the flow and the H axis to that of the velocity gradient, the velocity field is written as $\boldsymbol{v} = E(H)\boldsymbol{e}_x$, with $E(H) = WH$ (see figure 2). The $(G\text{-}H)$ plane corresponds to the shear plane and the I axis to the vorticity axis. A single operating parameter characterises this plane flow, the intensity of the shear rate W. This corresponds for the RBC to a hydrodynamic strength characterised by a viscous constraint $g = [_{ext}W$, where

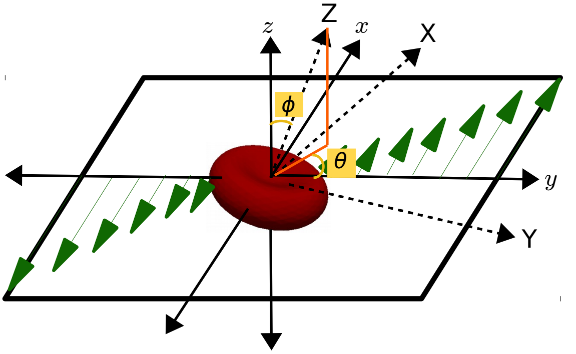

Figure 2 – Shear flow configuration((G- H- I) frame) with an RBC (($-$- $.$ - $/$) frame).

$[_{ext}$ is the viscosity of the external fluid. Successive experimental studies have continued to enrich the range of responses of the RBC to this very simple flow. One of the latest (Minetti *et al.* 2019) gives a summary of the experimental observations.

Basically, the dynamics of a rigid ellipsoidal object in this type of creeping flow is already extremely complex. The surface of such an object satisfies an equation of the form $-^2 + .^2 + A^2/^2 = 1$. Prolate and oblate ellipsoids are characterised by aspect ratios A Ÿ 1 and A ¡ 1, respectively. Between the two, $A = 1$ corresponds to a sphere. Let q be the orbit angle, i.e. the angle between the vorticity axis of the flow (I axis) and the symmetry axis of the object ($/$ axis). Let $\backslash$ be the angle of inclination, i.e. between the direction of the velocity gradient (H axis) and the projection in the shear plane of the axis of symmetry of the object. Jeffery's theory of orbits gives the following time evolution law for these two angles (Jeffery 1922)

$$A \tan q = \frac{^{orbit}}{\sqrt{A^{-2}2>B^2\backslash + B8=^2\backslash}} \quad - \quad A \tan \backslash = \tan \frac{WC}{A + A^{-1}} \tag{3.1}$$

The parameter $^{orbit} = A \tan q_0$ is the orbit parameter. In Jeffery's theory, all orbits are probable, determined only by the initial value q_0 of the angle q. The rolling dynamic (RO) corresponds to the minimum value that ^{orbit} can take, i.e. 0 when $q_0 = 0$. In this case, the axis of symmetry of the object remains aligned with the axis of vorticity of the flow and the angle $\backslash$ is indeterminate. The object adopts a rigid solid rotation respecting its axis of symmetry. The tumbling dynamics (TU) corresponds to the other extreme case, when ^{orbit} tends towards infinity for $q_0 = c/2$. The axis of symmetry of the object remains in the shear plane and the angle $\backslash$ varies periodically between $-c/2$ and $c/2$. The object tumbles in the shear plane at the frequency $W/(A + A^{-1})c$. In the most general case (0 Ÿ ^{orbit} Ÿ ∞), the motion is more difficult to describe, with a precession of its symmetry axis around the vorticity axis of the flow. Moreover, the orbit angle varies between q_0 for $\backslash = \pm c/2$ and a value more or less large according to the value of A and which is reached for $\backslash = 0$. This more general dynamic is the flipping (FL), with the TU and RO as extreme particular cases.

The resting shape of a normal RBC is the discocyte, whose convex envelope is an oblate. However, its great capacity to deform makes the problem much more complex. The characterisation of its dynamics requires consideration of its properties as a soft object, in addition to the characteristics of the flow. The first element determining its rigidity is the viscosity contrast $\_ = [_{int}/[_{ext}$, the relative value of its internal viscosity to that of the external fluid. Under physiological conditions, it is greater than unity since the viscosity of the cytosol of a healthy RBC can vary from 6 to 20 mPa s (Mohandas & Gallagher 2008; Williams & Morris 2009), whereas that of the plasma is only of the order of 1•5 mPa s (between 1 and 1.3 at body temperature (Késmárky *et al.* 2008)). The value of 6 mPa s is generally considered to be characteristic of a young and healthy RBC at body temperature (10 mPa s at room temperature). However, the majority of experimental studies have been carried out with much more viscous fluids, with characteristic viscosity contrasts below unity. The second key factor is the elastic properties of the RBC membrane. The contribution of the SC, characterised by its shear modulus μ, is recognised as dominant. As for the contribution of the viscosity of the cytosol, its action must be compared to that of the hydrodynamic strength, hence the introduction of the capillary number $Ca(\dot{\gamma}, \mu) = \eta_{ext}\dot{\gamma}R/\mu$. It is the ratio of the viscous stress $\sigma = \eta_{ext}\dot{\gamma}$ which characterises the hydrodynamic strength and the quantity μ/R which characterises the intensity of the elastic response of the SC. The size of the RBC is characterised by its equivalent radius R, the radius of the sphere with the same volume as the RBC. The typical value shown in Table 1 of (Levant & Steinberg 2016) is 2·82 µm. Considering all these characteristic elements of the FSI problem, the dynamic regimes can be listed in the plan $(\lambda, Ca(\dot{\gamma}, \mu))$, often referred to as the phase diagram.

In a numerical study, it is possible to vary all the properties involved. It is therefore essential to present the results in terms of these two characteristic dimensionless numbers. In an experimental study, the physical properties of RBCs are imposed by the sample at hand. In other words, the only parameters that it is convenient to vary in an experiment with the same sample are the shear rate $\dot{\gamma}$ and the viscosity η_{ext} of the bulk fluid. This explains why the results have most often been presented in the $(\eta_{ext}, \dot{\gamma})$ plane. However, it is underligned in (Minetti *et al.* 2019) that what is decisive for the RBC is the viscous stress and not the shear rate itself. Thus, the summary of the experimental observations made in (Minetti *et al.* 2019) translates into a phase diagram in the $(\eta_{ext}, \sigma = \eta_{ext}\dot{\gamma})$ plane (see figure 3 in (Minetti *et al.* 2019)).

Note that the dynamics of a capsule in shear flow is similarly characterised by a phase diagram in the $(\lambda, Ca(\dot{\gamma}, \mu))$ plane. On the other hand, for a vesicle that does not exhibit any shear elasticity, the reference elastic property is the bending modulus κ_c. The capillary number to use is thus $Ca(\dot{\gamma}, \kappa_c) = \eta_{ext}\dot{\gamma}R^3/\kappa_c = Ca(\dot{\gamma}, \mu)/\kappa_c^*$. The Von Karman number $\kappa_c^* = \kappa_c/R^2\mu = (\kappa_c/R^3)/(\mu/R)$ reflects the importance of the curvature elasticity (out of plane) relative to the shear elasticity (in plane). For an RBC, it is of the order of 5×10^{-3} (based on the average RBC property values shown in Table 1 of (Levant & Steinberg 2016)).

The description of the highly complex dynamics of an RBC in a shear flow is facilitated by limiting the studies to the case where the axis of symmetry of the RBC remains in the shear plane ($\Gamma^{orbit} = \infty$). The dynamics of the RBC can then be characterised by only two parameters. The first is the inclination angle θ which characterises the overall rotation of the RBC around the vorticity axis of the flow. The second is the Taylor deformation parameter D which characterises the intensity of the deformation undergone by the RBC. At low values of σ, the observed dynamics is the TU. The RBC tumbles like its rigid counterpart around the vorticity axis, the angle θ varying periodically between $-\pi/2$ and $+\pi/2$. This spinning motion is accompanied by a small deformation of the RBC. The Taylor deformation parameter varies with the same period and with an amplitude that increases with σ. At high σ values, the dynamics adopted is tank treading (TT), the name referring to the tank track motion of the RBC membrane. The inclination angle and the Taylor parameter take constant values. As σ increases, the axis of symmetry of the RBC moves closer to the direction of the velocity gradient and the deformation becomes more intense. In fact, the inclination angle does not take really a constant value. It exhibits periodic variations around its mean value but the amplitude decreases with increasing σ. The Taylor parameter presents small variations around its average value, with the same period. This dynamics is named swinging (SW) (Levant & Steinberg 2016).

For our purpose of comparing modelling strategies, this simplicity of description is a clear advantage. However, experimental studies indicate that the $^{orbit} = \infty$ orbit is not the most stable. An increase in the shear rate is more likely to be accompanied by a drift of the symmetry axis out of the shear plane. The transition from TU to TT then passes through the RO. The explanation given in (Dupire *et al.* 2012) is that the drift towards the RO is a path that allows the RBC to limit its deformations. On the other hand, when the transition study is performed by decreasing the shear rate instead of increasing it, the direct TT to TU transition is more present. In fact, this region of the phase diagram located in the vicinity of the $O_c(W\text{-}\,`)$ curve is associated with a hysteresis phenomenon. The curve $O_c(W\text{-}\,`)$ corresponds to the critical value of the capillary number for the transition to TT as a function of $\_$, or of $[_{ext}$ at a fixed $[_{int}$. The determination of this curve was the aim of the experimental study of Fischer & Korzeniewski (2013). This was a study on RBC populations with the criterion of half of the RBCs that have switched from one regime to the other. This became a baseline for all subsequent studies. Now, the g_c^+ value of viscous stress for which the transition is achieved by increasing the shear rate W is greater than the g_c^- value where the TT disappears by decreasing W. This is a phenomenon that has been at least observed when studying a population of RBCs (Minetti *et al.* 2019). It also corresponds to an intermittent regime (INT), where the dynamics of TT and TU mix and where the RBC undergoes greater deformations. This last phenomenon was highlighted even when working with a single cell (Levant & Steinberg 2016). It should be noted that this route to transition is observed for high values of suspension fluid viscosity, when $[_{ext}$ ¡ 20. From this value, the $O_c(W\text{-}\,`)$ curve reaches its minimum by becoming almost horizontal (Fischer & Korzeniewski 2013). It is with regard to this minimum value of the critical capillary, as well as the existence of the intermittency region, that the controversy over the reference shape of the cytoskeleton arose, to explain the inability of numerical models to reproduce them faithfully (Levant & Steinberg 2016). By going towards the physiological values of $[_{ext}$, i.e. at $\_$ ¡ 1, the $O_c(W\text{-}\,`)$ curve increases strongly and the transition can only be reached by imposing very high shear rates. Before reaching the transition, the RBC then undergoes very strong deformations, with the appearance of new dynamic regimes showing RBCs with stomatocyte and then multilobe shapes (Mauer *et al.* 2018). The choice to restrict our comparative study by assuming that the axis of symmetry of the RBC remains in the shear plane can be justified however. Our aim is not to cover the entire phase diagram and to study the transition routes. Rather, it is to compare the modelling strategies at points in the phase diagram that are representative of the dynamics of the RBC.

A first very strong argument to legitimise our approach is provided by the study (Levant & Steinberg 2016). It demonstrates that even experimentally it is possible to restrict oneself to this simpler configuration by exploiting the relationship between a simple shear flow and a plane linear flow. Keeping our choice of axes, the velocity field of the plane linear flow of parameters $(B\text{-}\,I)$ is written $\boldsymbol{v} = E_x(H)\boldsymbol{e}_x + E_y(G)\boldsymbol{e}_y$, with $E_x(H) = (B - I)H$ and $E_y(G) = (B + I)G$. A decomposition of the velocity gradient into symmetric and antisymmetric parts shows that $B = {}_{xy} = {}_{yx}$ is the only non-zero component of the strain rate tensor $\boldsymbol{D}$, whereas $I = -\Omega_{xy} = \Omega_{yx}$ is the only non-zero component of the rotation rate tensor $\boldsymbol{\Omega}$. Note that $I = I_z$ is also the only non-zero component of the vorticity vector, carried by $\boldsymbol{e}_z$. The plane linear flow is more general than the simple shear flow, to which it is reduced if $2B = 2I = W$. However, even when this condition is not met, the dynamics are similar. The results in plane linear flow can enrich the phase diagram in simple shear, provided that the effective viscosity $[_{ext} I/B$ is used. The plane linear flow is obtained in (Levant & Steinberg 2016) with a microfluidic equivalent of the Taylor four-roll mill system. It has the advantage of being able to trap an RBC in the observation zone for a comfortable time relative to the characteristic time of the RBC dynamics, under the condition I ¡ B. The study of the transition between the different dynamic regimes is controlled by varying B and therefore

I/B, at a fixed $\_$. The impact of increasing the contribution of I relative to B is that the path followed in the phase diagram is not accompanied by a drift of the axis of symmetry of the RBC out of the shear plane (see figure 2 of (Levant & Steinberg 2016)).

The results of (Levant & Steinberg 2016) are included in the survey of (Minetti *et al.* 2019) (see the phase diagram of figure 3). All points associated with the INT regime are located in the region [$0^{-} \approx 10^{-2}$- $0^{+} \approx 10^{-1}$] for an effective viscosity $[_{ext}B/I$ between 10^1 and 10^2 mPa s. This confirms the previous observations of (Dupire *et al.* 2012), except for the intensity of the RBC deformation, which was observed to be more consistent in (Levant & Steinberg 2016) as in (Dupire *et al.* 2012). Below 0^{-} and for effective viscosities $[_{ext}B/I$ decreased to 2 mPa s, only the TU appears. Above 0^{+} and for effective viscosities $[_{ext}B/I$ higher than 20 mPa s and lower than 100 mPa s, only the SW is present. Between 0^{-} and 0^{+}, both regimes are present. Note that the actual viscosity values considered for the external fluid are in the range [20- 86•5] mPa s. For $I/B = 1$ and a typical value of $[_{int} = 10$ mPa s, the corresponding viscosity contrast $\_ = [_{int}/[_{ext}$ is between 0•1 and 0•5. However, by considering $I/B \neq 1$, the study could be carried out up to an effective viscosity $[_{ext}B/I$ of the order of 2 mPa s, i.e. an effective viscosity contrast of 5, close to the physiological conditions. For these values of viscosity contrast greater than unity, all the values of capillary number considered were lower than 0^{-} and only the TU regime was observed.

Even if we remain in the shear flow configuration, which is the choice for the present study, our approach can be justified by a judicious selection of the study points. A first argument is that the transition to decreasing shear rate does not necessarily pass through the RO regime. A second argument is that the characteristic drift time of the RBC symmetry axis out of the shear plane would vary as $[_{ext}/W$ (Levant & Steinberg 2016). It can therefore be large relative to the time scale of the RBC dynamics for $[_{ext}$ large and W small, i.e. for $\_ \ddot{Y} 1$. It has also been shown in (Minetti *et al.* 2019), under physiological conditions, that the range of stable orbits widens as the shear rate decreases. The orbit $^{orbit} = \infty$ becomes stable below a certain value of g, of the order of 10^{-2} Pa (see figure 14(c) in (Minetti *et al.* 2019)). It is highlighted in (Minetti *et al.* 2019) that the trend is the same at low and high values of $[_{ext}$, provided that we reason in viscous stress $g = [_{ext}W$. Simply, it is easier to explore the low g region when $[_{ext}$ is small, especially in physiological conditions. This is the case of the studies conducted in (Minetti *et al.* 2019), where the physiological value $[_{ext} = 1•5$ mPa s was considered, in addition to the value 25 mPa s which is closer to the values considered in most previous studies. On the other hand, as already mentioned, the $0_c(W\text{- }`)$ curve reaches its minimum as soon as $[_{ext}$ is greater than 20 mPa s. It is therefore easier to reach the TT regime at high values of $[_{ext}$. In this last regime, the study (Minetti *et al.* 2019) revealed two dominant and equiprobable orientations of the RBC symmetry axis, along the vorticity axis or in the shear plane (see figure 16(a) of (Minetti *et al.* 2019)).

In order to cover the most characteristic dynamic regimes of an RBC in shear flow, our comparative study focuses on four points of the phase diagram. The first one corresponds to the TU, under physiological conditions to ensure the stability of the orbit $^{orbit} = \infty$. The second corresponds to the SW/TT, at $[_{ext}$ higher than 20 mPa s and considering the two possible orientations of the axis of symmetry of the RBC, aligned with the axis of vorticity or in the shear plane. The third is located in the intermittency region with coexistence of TU and SW/TT dynamics. Finally, the last one, in physiological condition but with a high shear rate, was chosen in order to be able to compare modelling strategies in the regime of very high deformations. In order to facilitate the reading of the results of the comparative study, the following colour code is used for all figures

C → Blue   C-S → Green   C-C → Cyan   V → Black   V-S → Orange   V-C → Red

Apart from the dimensionless numbers that characterise a study point in the phase diagram,

Property (units)	Used values	Dimensionless input (R, μ, η_{ext})
Surface Area, A (μm^2)	135	—
Volume, V (μm^3)	94	—
Sphericity	0.74	—
Reduced volume	0.64	—
Dimple thickness, h_D (μm)	1.4	—
Rim thickness, h_R (μm)	2.6	—
Effective radius, R (μm)	2.82063191	1
Bending rigidity, ${}_c$ ($\times 10^{-19}$J)	2.4	${}_c^* = {}_c/\mu R^2$
Shear elasticity, μ (μN m^{-1})	6.0	1
Friction coefficient per area, ${}_f$ (pN s μm^{-3})	144.0	${}_f^* = {}_f R/\eta_{ext}$
Cytoplasm viscosity, η_{int} ($\times 10^{-3}$Pa s)	10.0	$\lambda = \eta_{int}/\eta_{ext}$
Shear rate, $\dot{\gamma}$ (s^{-1})	—	$Ca = \eta_{ext} R \dot{\gamma}/\mu$
Time, t (s)	—	$t^* = t\mu/\eta_{ext} R$

Table 1 – Physical properties considered and dimensionless input data.

the other input data for the computation are given in the last column of table 1. In fact, our simulations are always performed in normalised quantities (indicated by a star throughout) with dimensionless input data. For normalisation, we use as a length reference scale the RBC equivalent radius $L_{ref} = R$ and as a time reference scale $t_{ref} = \eta_{ext} R/\mu$. Note that with this last choice, the capillary number is more simply defined as $Ca(\dot{\gamma}, \mu) = \dot{\gamma} t_{ref}$. All the quantities having dimension of a force surface density are normalized by the reference elastic stress $\sigma_{ref} = \mu/R$. Thus the real values of μ and ${}_c$ are never given. The former is specified via the capillary number $Ca(\dot{\gamma}, \mu) = \eta_{ext}\dot{\gamma}/\sigma_{ref} = \sigma/\sigma_{ref}$ and the latter via the Von Karmann number ${}_c^* = ({}_c/R^3)/\sigma_{ref}$. The input data of the table 1 are constructed with this convention. However, in order to be able to compare with the results of the literature, usually presented in real quantities in experimental studies, we indicate also in table 1 the properties we considered to perform the transformation. These data are inspired by averages of recognised values for a healthy RBC (see for example table 1 in (Levant & Steinberg 2016)). Finally, a last important property for the mechanics of RBCs concerns the reference shape of the SC. We have chosen the quasi-spherical shape with a sphericity of 0•96 rather than the discoidal shape, in the current trend in numerical modelling of RBCs. However, we kept a zero spontaneous curvature. The sensitivity of our results to this choice is an aspect that is addressed in our discussion section.

3.1. *Effect of modelling strategy on tumbling dynamics*

This point of study is in physiological conditions (η_{ext} = 1•5 mPa s) and low shear rate (σ = 0•01 Pa). It corresponds to the characteristic dimensionless numbers λ = 6•667 and $Ca(\dot{\gamma}, \mu) = 5 \times 10^{-3}$. For this configuration, the V-S model diverges rapidly. The membrane surface loses its regularity under the influence of the anisotropy of the coarse spring network. Defects accumulate in the absence of any membrane elasticity other than curvature. This phenomenon is illustrated in the inset of figure 3 which shows the shape of the RBC obtained with the V-S model at a time step before divergence.

The other models are compared on figure 3 for the inclination angle and figure 4 for the Taylor deformation parameter. The evolution of the inclination angle clearly highlights the TU dynamics. It is characterised by the spinning frequency of the RBC around the vorticity axis. This frequency is the highest for C and C-S, and is almost identical for these two models.

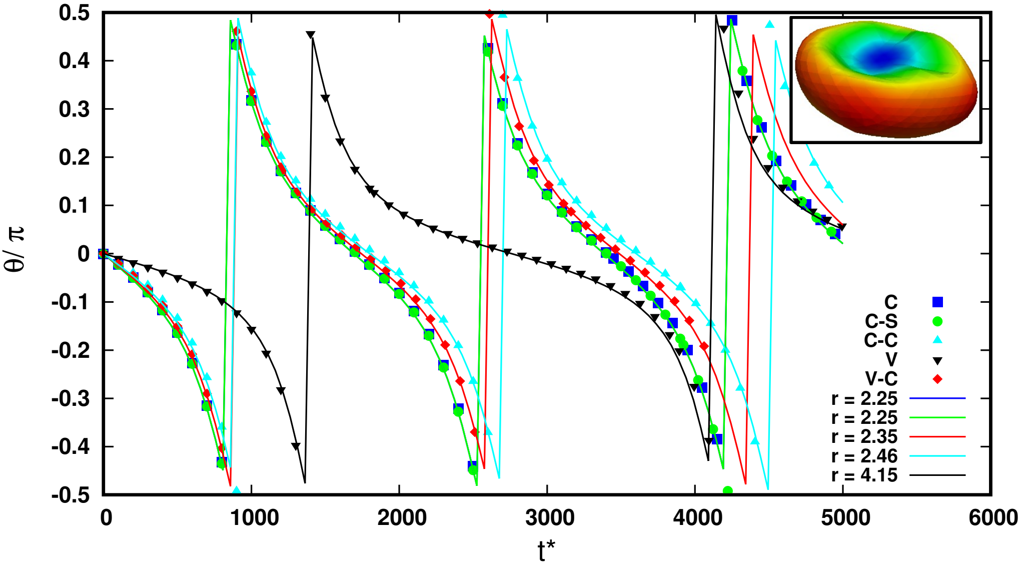

FIGURE 3 – Comparison of inclination angles on TU dynamics (_ = 6•667- 0(W- `) = 0•005). Points : simulations, solid line : Jeffery's theory for fitted A on frequency criteria. Inset : snapshot of V-S model showing the anisotropy and roughness on the membrane leading to divergence.

It is slightly lower for the C-C model and in between for the V-C model. The V model shows a spinning frequency almost half that of the other models.

The discrimination of the models is most evident in the comparison of the Taylor parameter. It shows that there is a direct relationship between the stiffness of an object and its spinning frequency. This relationship is not linear. The difference in stiffness between the C and C-S models is of the same order as between the C-C and V-C models. However, the influence on the spinning frequency is hardly visible for the first two models. It is more significant for the last two models because they show a greater overall deformation intensity than the first two. The phenomenon is further amplified for the vesicle which has no shear elasticity. Note the importance of rigorously considering the surface incompressibility constraint, with its stiffening effect well highlighted by the comparison between the C-C and V-C models.

Due to the small deformation of the RBC, this dynamic regime is close to that of a rigid particle. Indeed, it is stated in (Minetti *et al.* 2019) that Jeffery's theory is fairly well verified. For comparison, we also show in solid lines on figure 3 the curves obtained with Jeffery's theory ((3.1) second equation). For each modelling strategy, the aspect ratio A used is specified. This value of A is determined so as to tune the frequency to that of the model.

3.2. *Effect of modelling strategy on swinging dynamics*

This point of study is with an increased external viscosity ($[_{ext}$ = 25 mPa s) and high shear rate (g = 1•06 Pa). It corresponds to the characteristic dimensionless numbers _ = 0•4 and 0(W- `) = 0•5. For this configuration, the V-S model is not stable and diverges immediately. The comparison of the other models is shown in figures 5 and 6 for the case where the RBC is oriented at the initial time with its axis of symmetry in the shear plane.

For the other case, when the symmetry axis is initially aligned with the vorticity axis, the dynamics only differ during a short transient period. the RBC adapts its shape to eventually adopt a similar dynamic to that observed for the first configuration. Figure 7 shows the effect of the modelling strategy on the evolution of the RBC shape during this transitional phase.

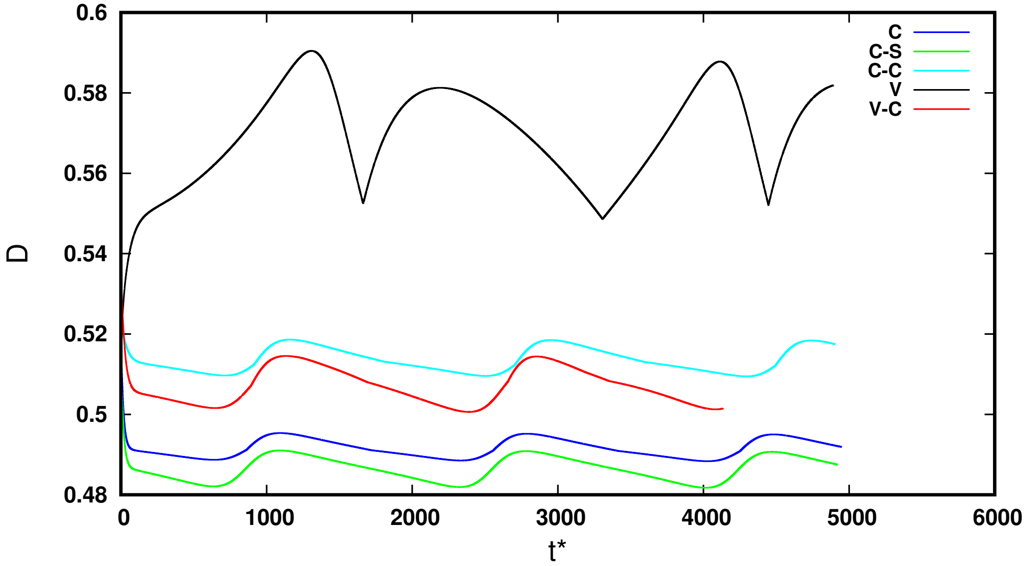

Figure 4 – Comparison of deformations on TU dynamics (_ = 6•667- $O(W\text{-}\,`)$ = 0•005).

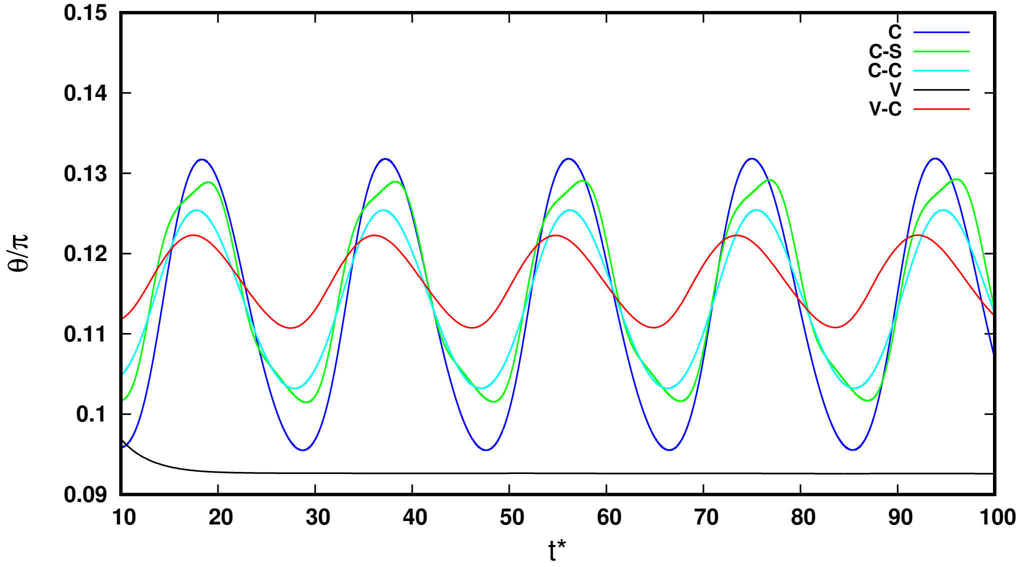

Figure 5 – Comparison of inclination angles on SW/TT dynamics (_ = 0•4- $O(W\text{-}\,`)$ = 0•5), when the RBC's symmetry axis is initially in the shear plane.

All models follow broadly the same transition pattern with equivalent relaxation times, except for the V model which undergoes a large deformation and then lengthens. However, some differences are noticeable. Here again, the same grouping of models can be made, with a similarity in behaviour for models C and C-S on the one hand and for models C-C and V-C on the other. A clear difference in behaviour between the two groups can notably be seen at $C^* = 11$, just before the end of this transitional phase. While models C and C-S still show a reversal of the curvature at $H = 0$ in the $(H\text{-}I)$ plane, models C-C and V-C no longer do.

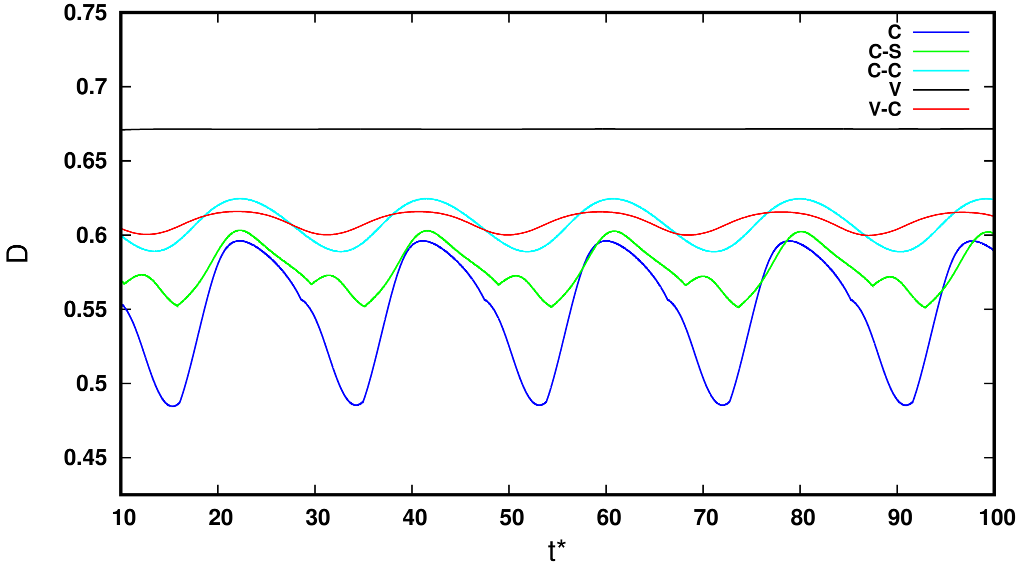

Figure 6 – Comparison of deformation on SW/TT dynamics (_ = 0•4- $O(W- `)$ = 0•5), when the RBC's symmetry axis is initially in the shear plane

Again, the absence of shear elasticity leads to a separate behaviour for the V model. For this model, the inversion of curvature at $H = 0$ disappears very early and no inversion of curvature ever appears at $I = 0$, unlike the other models.

With its axis of symmetry in the shear plane from the start, the RBC is already well oriented relative to its final steady state. The transient phase of large deformations is correspondingly reduced. The evolution of the shape of the RBC is given in figure 8.

Except during the transient phase, the dynamics are then identical, whatever the initial orientation of the symmetry axis, in the shear plane or aligned with the vorticity axis. With a normalized time shift of $\triangle C^* = 11•6$, the evolution curves of the figures 5 and 6 are indistinguishable from those obtained when the symmetry axis is aligned with the axis of vorticity. Since this are the two extreme cases, generalisation to any initial orientation is very likely. Once the steady state is reached, the evolution of the inclination angle shows that the SW is most pronounced for the C model and least pronounced for the V-C model. The C-S and C-C models are in between, with the SW a little more pronounced for the C-S model. As expected, the V model is in pure TT, characterised by a constant value of the inclination angle. Once again, it is the evolution of the deformation via the Taylor parameter that best allows the models to be distinguished. The same grouping, with models C and C-S on the one hand and models C-C and V-C on the other, is also obvious here. The V model is completely separate and as expected has the most intense deformation. The C-C and V-C models produce mean deformations of the same order, with an almost sinusoidal regularity of the Taylor parameter evolution. The stiffness provided by the surface incompressibility is nevertheless reflected in an oscillation amplitude half as large for the V-C model as for the C-C model. The mean deformation intensity is lower for the C model but with an oscillation amplitude two to three times greater than for the C-C model. In addition, the oscillations appear to be much less symmetrical, with even the beginnings of a rebound in the decreasing phase. The evolution curve of the C-S model wraps relatively well around the top of the C model one, before the shift induced by the slight difference in frequency becomes too great.

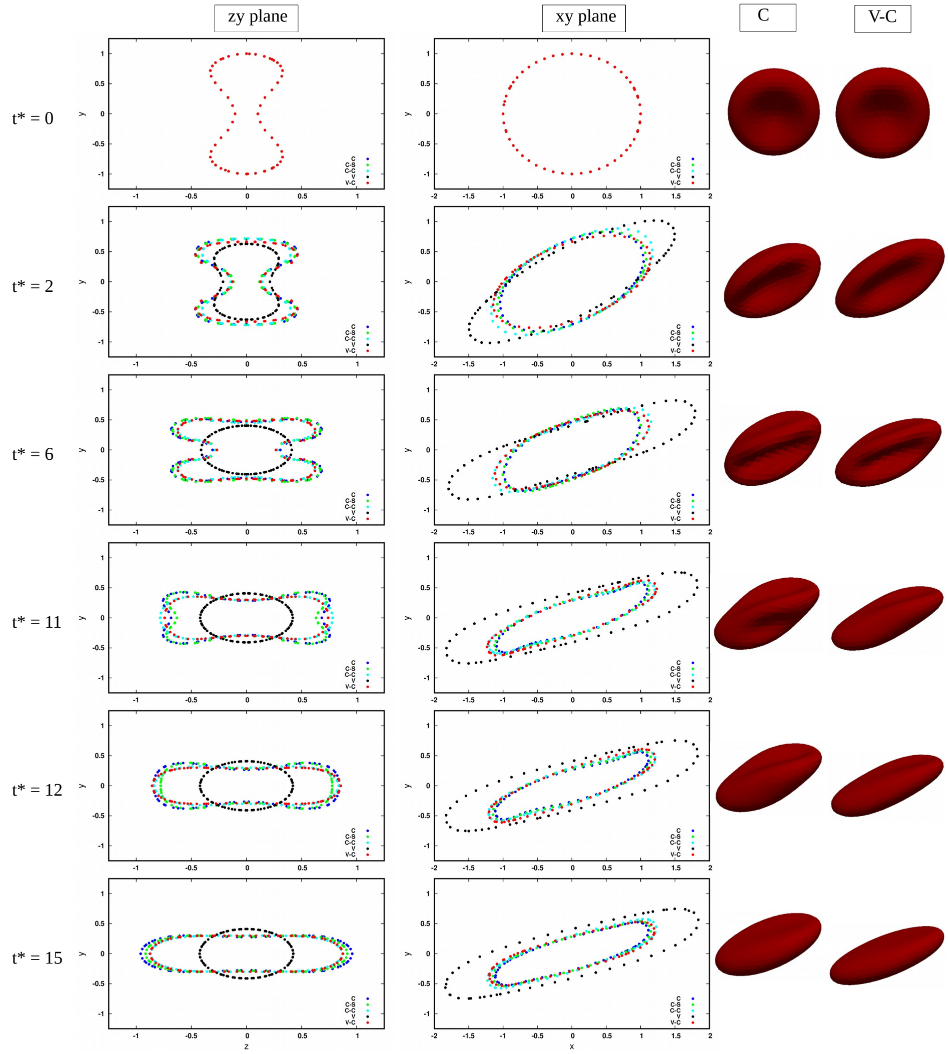

FIGURE 7 – Comparison of shape evolutions on SW/TT dynamics (_ = 0•4- O(W- `) = 0•5) in the transient phase for the case when the RBC's symmetry axis is initially aligned with the axis of vorticity. First columns : (z,y) and (x,y) plane sectional drawing, last columns : 3D view for the C and V-C models.

The rebound is this time well marked and could explain the half lower amplitude but with a higher average value than for model C.

Figure 9 compares the shape evolutions of the RBC in the established regime. The V model undergoes a much larger deformation and is not considered for this reason. The very similar shape obtained with the C-C and V-C models is relatively stable, compared to the strong shape variations obtained with the C model. In cross-section in the shear plane, the evolution for the latter periodically changes from an elliptical to an S-shape (breathing phenomenon). It should be noted that on the basis of the shear plane section, the C-S model could be closer to the C-C and V-C models than to the C model. However, a slight breathing phenomenon is already noticeable.

A legitimate question is whether the transitional phase in the case where the axis of

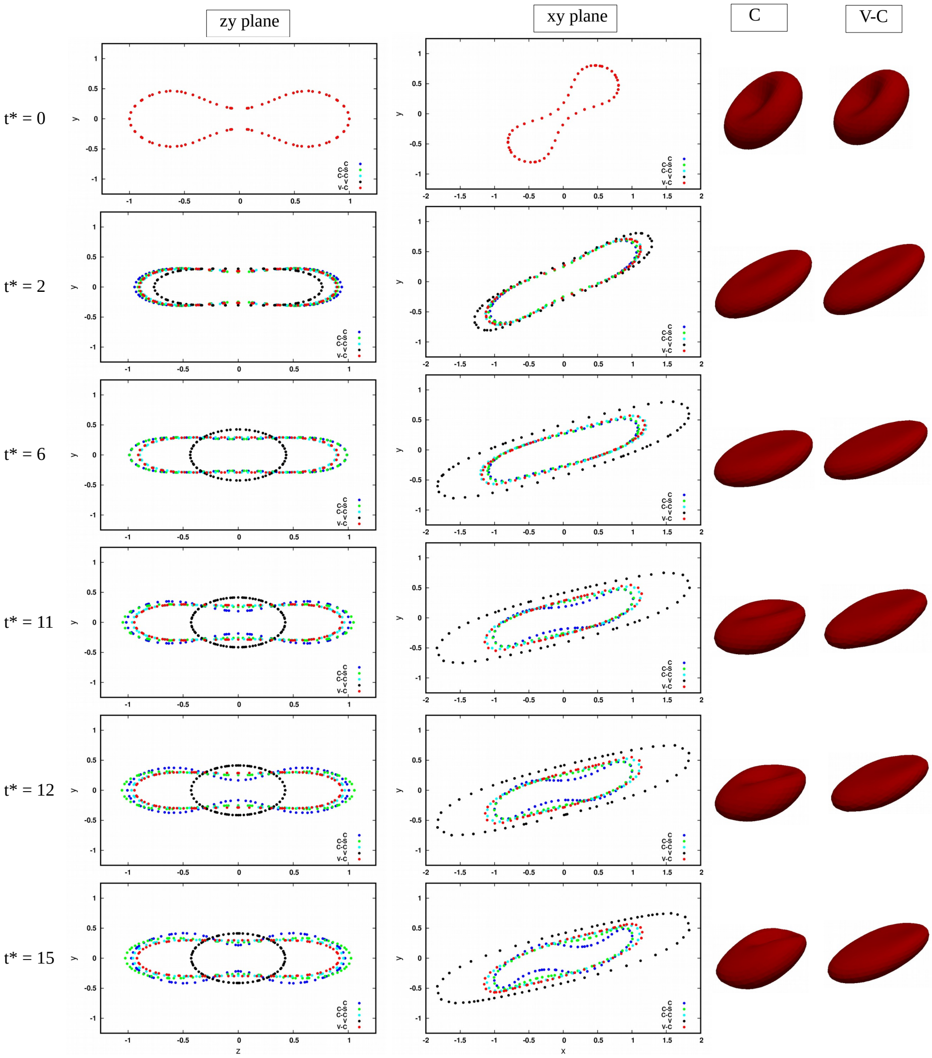

FIGURE 8 – Comparison of shape evolutions on SW/TT dynamics (_ = 0•4- O(W- `) = 0•5) in the transition phase when the RBC's symmetry axis is in the shear plane at start. First columns : (z,y) and (x,y) plane sectional drawing, last columns : 3D view for the C and V-C models.

symmetry is aligned with the axis of vorticity is only a shape adaptation or whether it is accompanied by a general tangential movement of the SC. If the answer is negative, the final state reached cannot be considered as completely identical to the one reached starting from the other orientation, at least from the energetic point of view. To know this, it is sufficient to follow the evolution of the H coordinate of two markers, one initially located on the dimple in the centre of one of the two faces of the RBC and the second on the periphery. For the latter, we choose one of the two intersections with the $(H- I)$ plane at the initial time, i.e. with a coordinate $H = 0$. It clearly showed that the answer is negative. When the axis of symmetry is initially in the shear plane, it is the dimple that undergoes the TT movement. This rotational movement is about the vorticity axis and the H coordinate of the other marker remains almost zero, as expected. But when the axis of symmetry is initially aligned with

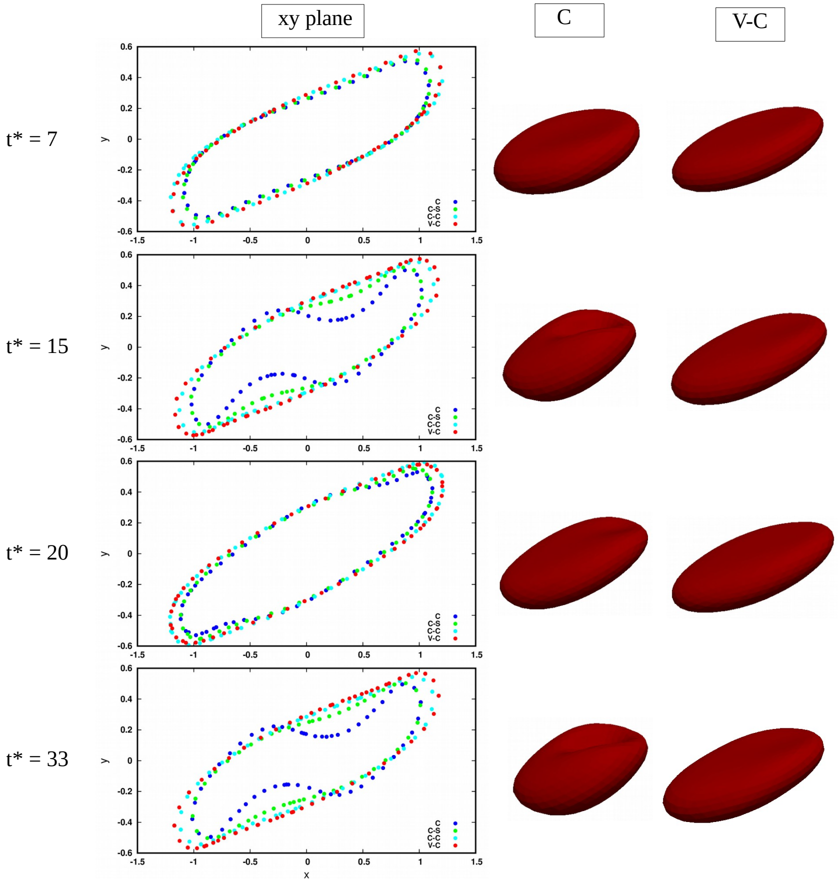

FIGURE 9 – Comparison of shape evolution on established SW/TT dynamics (_ = 0•4- $0(W\text{-}`)$ = 0•5), with normalized time corresponding to the case when the RBC's symmetry axis is initially in the shear plane. First column : (x,y) plane sectional drawing, last columns : 3D view for the C and V-C models.

the axis of vorticity, it is on the contrary the marker at the periphery that undergoes the TT motion. It also showed that there is an apparent increase in TT frequency of modelling the BL as an incompressible fluid film rather than a solid shell. However, it is difficult to conclude whether this is related to the consideration of the fluid nature of the BL or to the more rigorous treatment of the surface incompressibility constraint.

3.3. *Effect of modelling strategy on transition to tank-treading*

This point of study is located at the upper limit of the intermittency region when $[_{ext}$ = 24 mPa s. For this value of $[_{ext}$, the experimental study (Fischer & Korzeniewski 2013) identified a critical shear rate of W = 10 s^{-1} for the transition, i.e. a critical viscous stress of g = 0•24 Pa. The values of the corresponding characteristic dimensionless numbers are _ = 0•416667 and $0(W\text{-}`)$ = 0•11282528. Located in the transition zone, this is a point where the behaviour of the models should be particularly sensitive to the modelling strategy. This sensitivity is highlighted in figures 10 for the inclination angle and 11 for the Taylor deformation parameter. As the V-S model is unstable at this point of study also, it is not considered.

The V model is in pure TT, with a constant angle of inclination. The V-C and C-C models

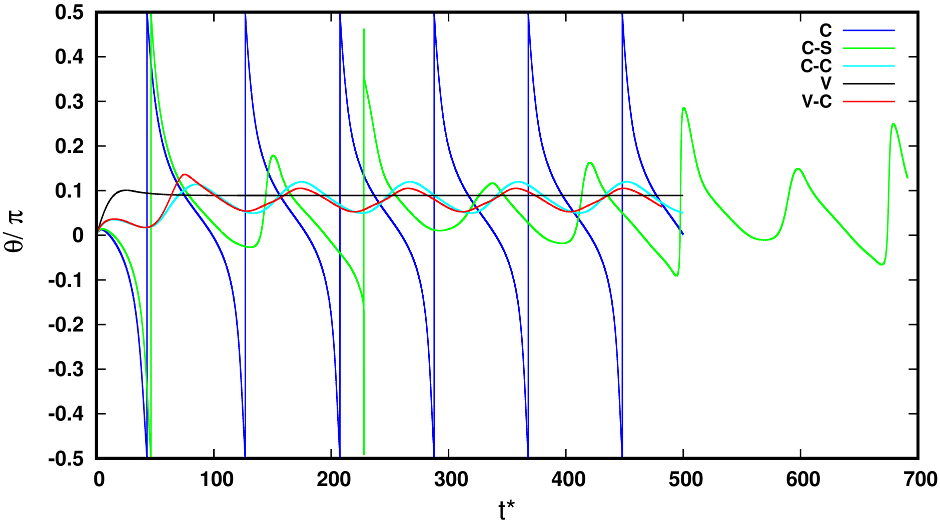

FIGURE 10 – Comparison of inclination angles in the TU to SW/TT transition region (_ = 0•416667- O(W- `) = 0•11282528).

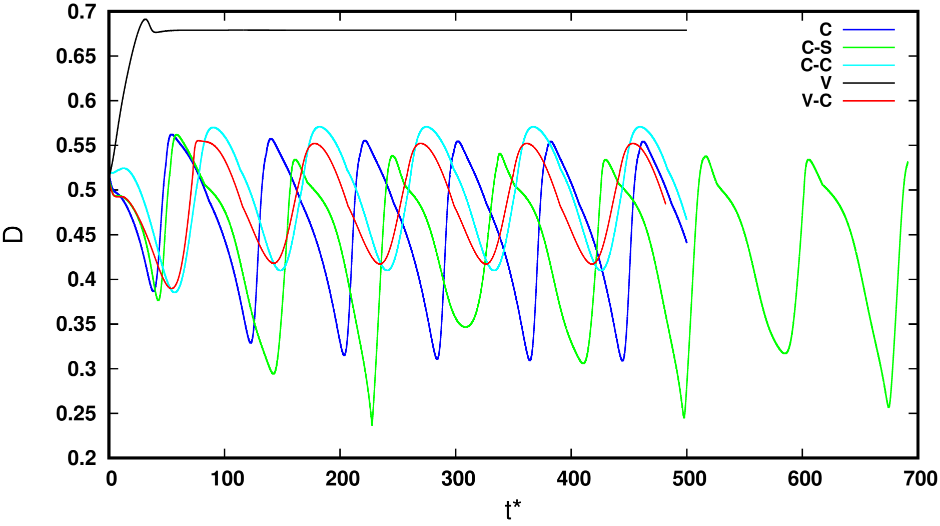

FIGURE 11 – Comparison of deformation in the TU to SW/TT transition region (_ = 0•416667- O(W- `) = 0•11282528).

have a very similar behaviour, showing a transition to SW/TT. After one or two periods, they adopt a permanent SW dynamic. Their inclination angle oscillates around a mean value close to that adopted by the V model, with a slightly larger amplitude for C-C model. The C-S model undergoes a transition after one cycle of TU and shows a huge variation in its dynamics. It is a combination of TU and SW/TT, associated with intermittence (INT) in (Levant & Steinberg 2016). Finally, the C model is always in the TU regime.

To distinguish the INT dynamics from the others, an alternative presentation of data is recommended in (Levant & Steinberg 2016). It consists in tracing the trajectory of the dynamical system in the phase plane (\/c-). In this presentation, TU and SW dynamics are

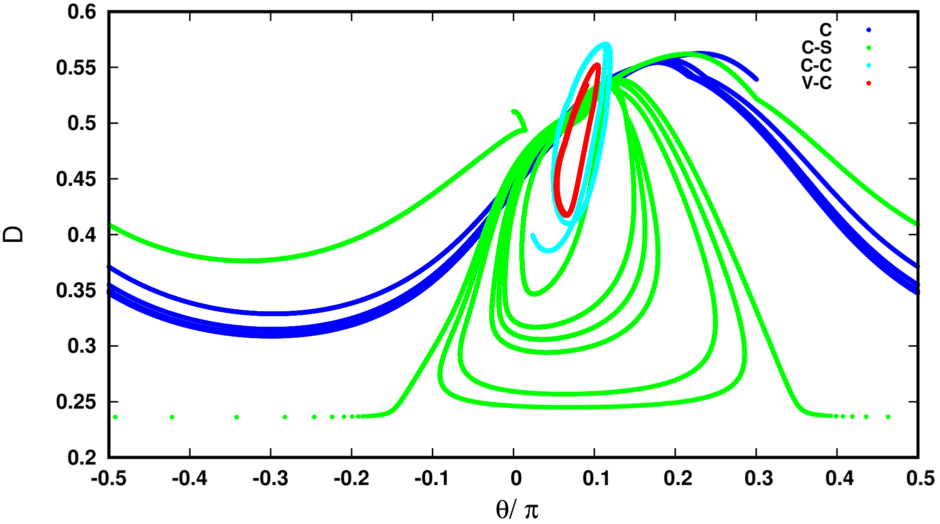

FIGURE 12 – Comparison of trajectories in the (\/c-) plane (_ = 0•416667- O(W- `) = 0•11282528).

distinguished by open trajectories and small limit cycles, respectively. The SW dynamics is characterised by large limit cycles, with rare excursions on open trajectories. This presentation is implemented in figure 12 for our comparison study, to be compared with figure 17 of (Levant & Steinberg 2016). It confirms our classification based on the figures 10 and 11.

3.4. *Effect of modelling strategy in high deformation regime*

This point of study corresponds to physiological conditions ($[_{ext}$ = 1•5 mPa s) but at high shear rates (g = 3•19 Pa). With the values of the physical properties of RBC given in table 1, the values of the characteristic dimensionless numbers are _ = 6•667 and O(W- `) = 1•5.

With very high viscosity contrast and capillary number, the RBC undergoes very large deformation and takes a multilobe shape, in agreement with (Mauer *et al.* 2018). The deformation parameter varies between a minimum and a maximum, in which the minima and maxima corresponds to different multilobe shapes. The deformation rate and the shape taken depends on the modelling strategy. The evolution curves of the inclination angle and the Taylor deformation parameter are compared in figures 13 et 14. Note that the V-S model is stable for this case while the V model diverges.

From the evolution of the Taylor deformation parameter, the association of the C-C and V-C models can again be made. If, as for the other study points, the results for the V-S model were lacking, we would combine the C-S model with the C model. Here we can refine the characterisation by grouping the C-S and V-S models. They are closer to the C model than to the C-C and V-C models, but are still different from the C model. It should be noted that the stiffening action of the surface incompressibility stress provided by the BL modelled as a vesicle is again clearly visible when the SC is modelled as a capsule. On the other hand, it is almost non-existent when the SC is modelled as a network of springs.

4. Discussion

The conclusion of our comparison is that there is indeed an impact of the choice of modelling strategy. We undertook this study to quantify this impact precisely but with the idea that it would probably be small. This prejudice was based on the fact that the community

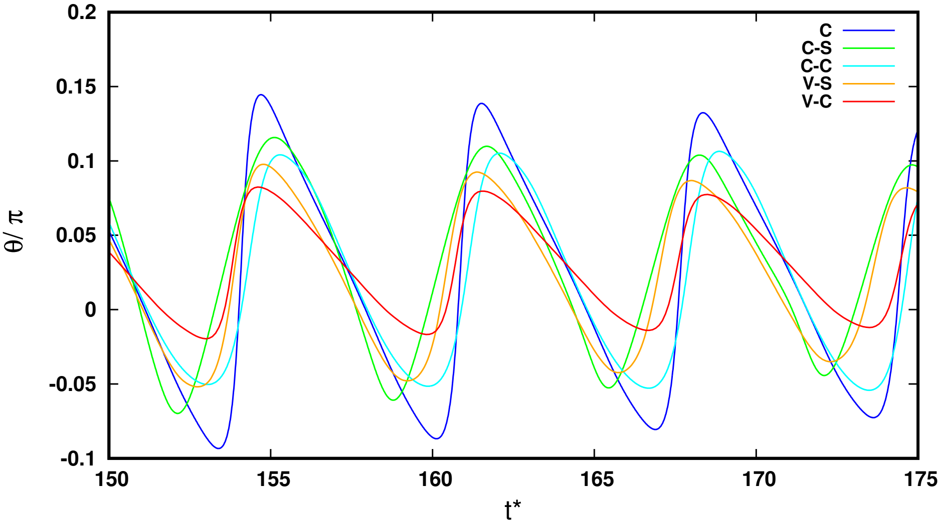

FIGURE 13 – Comparison of inclination angles in the multilobe region (_ = 6•667- O(W- `) = 1•5).

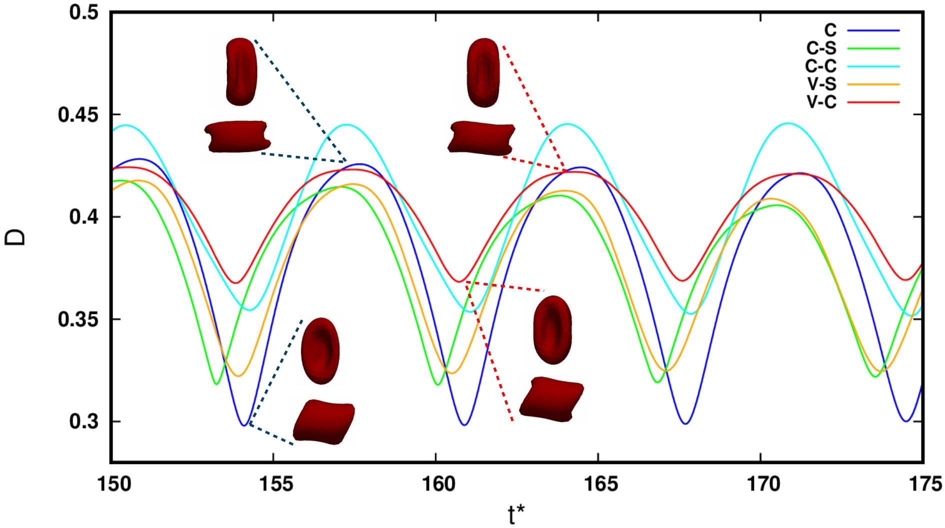

FIGURE 14 – Comparison of deformation in the multilobe region (_ = 6•667- O(W- `) = 1•5) with G axis view and I axis view of C model (left) and V-C model (right) when reaches its maximum (top) and minimum (bottom).

is used to comparing the results of numerical studies without really paying attention. This was evidenced by the discussion around the question of the reference shape of the SC which unanimously led to a preference for the quasi-spherical shape. It is true that the shear elasticity provided by the SC is decisive. In our study, the separate behaviour of the V model confirms this result. However, our study shows also that a model that distinguishes between the SC and the BL does not behave in the same way as one that models them as a block. Moreover, even in the first category, the way in which the SC is modelled, by a network of springs or by a capsule, is not without consequence. One way of judging the importance of this finding is to put it into perspective with the influence of the reference shape of the SC. Such a comparison

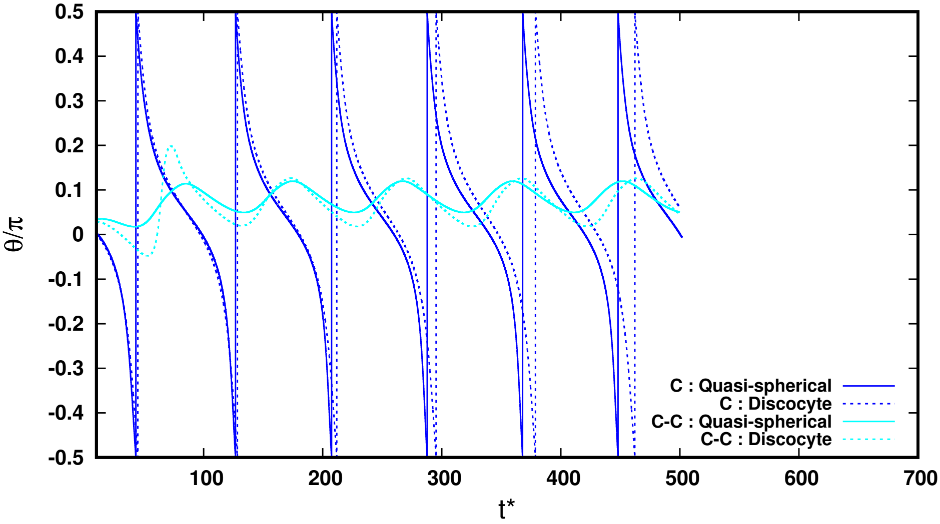

Figure 15 – Comparison of inclination angles in the TU-SW/TT transition region (_ = 0•416667- O(W- `) = 0•11282528) for the C and C-C models using two different reference shapes for the SC.

is given in figure 15 for the study point (_ = 0•416667- O(W- `) = 0•11282528), which is located in the transition to TT region. The sensitivity of models to the choice of the reference shape of the SC is recognised there. The comparison is carried out for the C and C-C models with two alternatives of reference shape, discocyte or quasi-spherical (sphericity of 0•96, already used). Zero spontaneous curvature is considered in all cases. For both modelling strategies, switching to the discocyte reference shape for the SC has the effect of slightly decreasing the oscillation frequency. For the C-C model, a slight increase in the amplitude of the oscillations is moreover visible. However, for neither strategy does the influence go so far as to change the nature of the dynamics. Model C remains in TU regime and model C-C in SW/TT. This is a result that leads us to conclude that distinguishing the SC from the BL modifies the dynamics more consistently than using a different reference shape for the SC.

Surprisingly, when pushing the comparison in the SW/TT regime, we observe a greater influence of the choice of the reference shape for the SC. The evolution curves of the inclination angle and the Taylor deformation parameter are given in figure 16. As a reminder, the evolution curves obtained with the quasi-spherical reference shape are shown in the inset. In addition, the shapes adopted by the RBC at $C^* = 48$ and $C^* = 52$ are compared in figure 17. The main consequence of this change of reference shape is that unlike the quasi-spherical shape, the discocyte shape induces an undeniable discrimination between the two cases of orientation of the RBC symmetry axis. This is true for both the C and the C-C model, but is even more radical for the latter. When the axis of symmetry of the RBC is initially in the shear plane, the influence remains weak. A slight increase in the amplitude of the oscillations of the inclination angle and the deformation parameter is observable for both models. This result seems to be consistent with the interpretation in terms of the energy barrier to be overcome to allow TT movement of the membrane when the axis of symmetry of the RBC is in the shear plane. This barrier is greater for the discoidal reference shape than for the quasi-spherical shape. When the axis of symmetry of the RBC is aligned with the axis of vorticity, this energy barrier no longer exists. In the case of the C-model, this results in a smaller oscillation amplitude for both the angle and the deformation and with a lower average deformation intensity. However, the most striking consequence is the doubling of

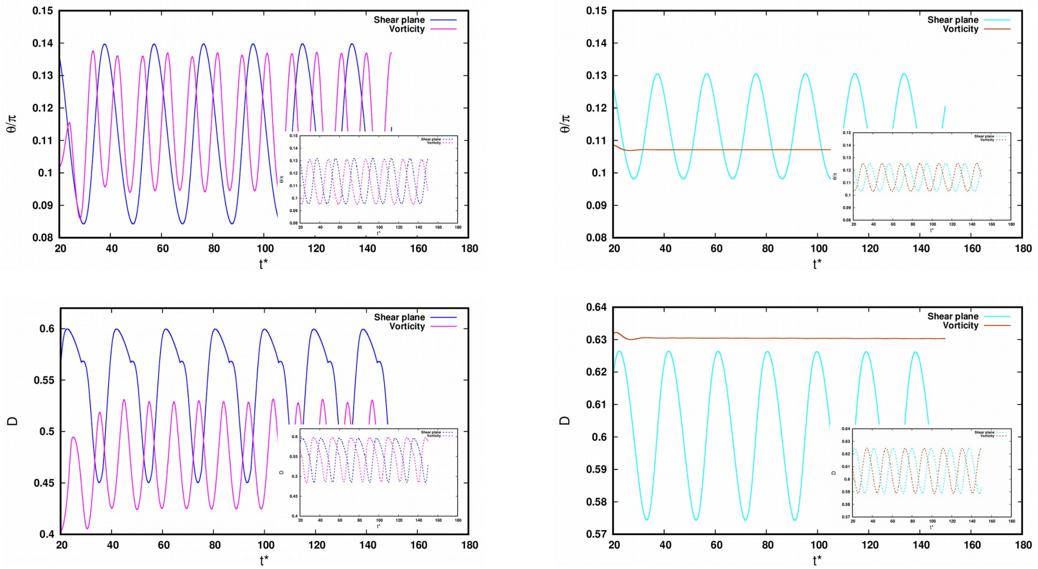

Figure 16 – Influence of the SC reference shape on inclination angle (top) and deformation (bottom) in SW/TT dynamics (_ = 0•4- 𝑂(𝑊- `) = 0•5), for C model (left) and C-C model (right). Inset : results with quasi-spherical reference shape, for recall.

the oscillation frequency. In the case of the C-C model, the change is even more radical. All points on the same TT path are mechanically equivalent when the axis of symmetry of the RBC is aligned with the axis of vorticity. The oscillations are thus no longer relevant. The inclination angle and the deformation parameter take a constant value, the RBC switches to pure TT dynamics. Note that the intensity of the deformation is increased, in contrast to model C. Thus, even in this case, the difference in modelling strategy between models C and C-C has a greater impact than a different choice for the reference shape of the RBC. Nevertheless, the two influences are working together. One point remains mysterious in this interpretation of the observations. Why does the SW dynamics not disappear systematically as soon as the symmetry axis is aligned with the vorticity axis, whatever the modelling strategy and whatever the reference shape of the SC ? The only explanation that comes to mind is a greater or lesser influence of the dimple from the axis of symmetry towards the periphery. The more marked the deviation from the sphere, the more robust the memory of the initial shape, leading to maintaining the location of the curved region around the axis of symmetry. A picture illustrating our idea is that of the rim of a car wheel, which is more rigid than the tyre, which can then deform more strongly but also more evenly.

Let's recall that from the fundamental aspect of our study, it is only the way models are combined that can be blamed for a difference in behaviour. This argument allows us to claim that our study is truly representative. Of course, any modelling choice is debatable, whether it concerns the numerical method adopted, the resolution algorithm or any other aspect of the numerical implementation. However, it will have an egal impact on all the modelling strategies we have compared. Even the influence of the value of a physical property cannot be put forward since it is the same used everywhere. No, the only possible sources of divergence lie in the way we combine our models.

Focusing on this aspect, a legitimate question concerns the contribution of surface viscosity

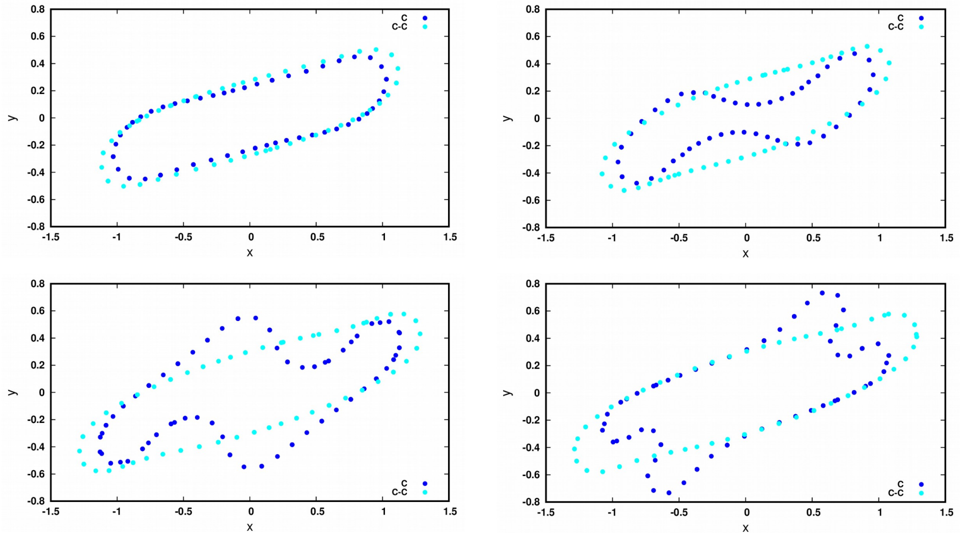

FIGURE 17 – Shape evolution with discocyte reference shape for the SC on SW/TT (_ = 0•4- $O(W-`)$ = 0•5), for C model and C-C model, at C^* = 48 (left) and C^* = 52 (right). The RBC's axis of symmetry is initially in the shear plane (top) or aligned with the axis of vorticity (bottom),

brought by the BL-SC coupling. Indeed, no such contribution has been considered for the V or C models. For the composite models, it is unavoidable since the BL-SC coupling is provided by the friction of the JCs in the BL. To what extent can the difference in behaviour between these two classes of models be explained by this additional contribution of surface viscosity ? A first answer is provided by the models with a SC materialized by a network of springs. Although reflected in point forces rather than surface density, the total intensity of friction between SC and BL is respected. However, their deviation from model C is much smaller, so that we have been led to group the C-S model with model C, rather than with models C-C and V-C. Another answer can be given by studying the sensitivity of the composite models to the value considered for the friction coefficient $_f$. In fact, doing this study by considering only one of the two models C-C or V-C is sufficient since they deviate the most from the C model. Moreover, these two models present a rather similar behaviour, with a well identified influence of the surface incompressibility constraint for the V-C Model. The choice of the C-C model for this study is therefore obvious. It remains to be established to what extent it is reasonable to vary the value of $_f$?

In order to stay close to biological reality and in accordance with the relation (2.22), it is appropriate to consider two ingredients, the typical friction coefficient $_{fJC}$ of a JC and the surface density d_{JC} of JCs. For our entire study so far, we have used the value $_f$ = 144 pN s μm^{-3} of Peng *et al.* (2011). In this study, the estimation is based on band-3 diffusion for actin JCs, combining three band-3s per JC, and Glycophorin-C diffusion for ankyrin JCs. However, in the analytical model of the more recent study of Turlier *et al.* (2016), a lower value was obtained with some modifications in the approach (see Supplementarory information S2.2 of Turlier *et al.* (2016)). Indeed, an experimental fact that allows not to distinguish the two types of JC is that the part of the complex located in the BL is in all cases dominated in size by band-3. It is then just the number of band-3s involved in each JC that counts, which can ultimately be translated in terms of junctional band-3s per spectrin tetramer. In (Turlier *et al.* 2016), three band-3s are associated with actin JCs, as in (Peng *et al.* 2011), but only one is considered for ankyrin JCs. Considering that an actin JC hosts six spectrin tetramers, each of these tetramers can then be associated with $1 + 2/6 = 4/3$ copies of band-3. It is then sufficient to multiply this $4/3$ value by the areal density of spectrin tetramers to obtain the areal density of band-3s attached to the SC. The value of $_f$ is then obtained using the coefficient of friction of band-3, instead that of a JC (i.e. $_f = d_{B3}\ _{f_{B3}}$). band-3 is the major protein of the RBC's membrane. It is in fact a dimer. One of the two constituent proteins, the one who is attached to the SC, is located in the cytosol. The second is located in the BL in the form of an anion channel that participates in the transport of carbon dioxide (Lux 2016). The coefficient of friction associated with the diffusion of band-3 into the BL is estimated as the inverse of its mobility via Einstein's relation $_{f_{B3}} = :_B)/\ _{s_{B3}}$. In this relation, $_{s_{B3}}$ is the free translational diffusion coefficient. In (Peng *et al.* 2011), an RBC in-situ measured value of $_{s_{B3}}$ was used. However, this value was considered too low in (Turlier *et al.* 2016), on the argument that the majority of band-3s cannot diffuse freely into the RBC membrane as they are attached to the SC. The alternative that was preferred is the estimation from the Saffman-Delbrück relationship (Saffman & Delbruck 1975), resulting in $_{s_{B3}} \sim 3{\cdot}8\ \mu\text{m}^2\ \text{s}^{-1}$ (see Supplementarory information S2.2 of Turlier *et al.* (2016)). Note that this value is very close to the value of $4\ \mu\text{m}^2\ \text{s}^{-1}$ used for glycophorin-C for ankyrin JCs in (Peng *et al.* 2011). However, it is about 180 times larger than the value of $_{f_{B3}}$ based on the measured value of $_{s_{B3}}$. Considering 45 000 spectrin tetramers for an RBC surface of 133•5 μ^2, as in (Turlier *et al.* 2016) (see Supplementarory table S1) we obtain a surface density of band-3 attached to the SC $d_{B3} \sim 450\ \mu\text{m}^{-2}$ and a surface coefficient of friction of $_f = d_{B3} :_B)/\ _{s_{B3}} \sim 0{\cdot}49$ pN s μm^{-3}, which is almost 300 times smaller than the one we have used so far. However, as mentioned in the introductory section, recent proteomic studies indicate that the density of intrinsic proteins, including band-3, would be much greater (Bryk & Wiśniewski 2017; Gautier *et al.* 2018). A number of 1•2 million of band-3s per RBC is already put forward in (Lux 2016), of which only 20-50% would not be recruited to a JC. Furthermore, there remains much uncertainty about the organisation in the BL of the protein complexes involved in JCs. The number of band-3 proteins involved in an ankyrin JC no longer seems to be in dispute. For the RBC membrane as a whole, this would represent 40% of the band-3 proteins recruited to ankyrin JCs (Lux 2016). In contrast, the number of band-3 proteins involved in an actin JC is not certain, varying from one to six. For the RBC membrane as a whole, this would represent 7-40% of the band-3 proteins recruited to actin JCs (Lux 2016). Hence the estimate of between 20% and 50% of band-3 proteins remaining free for the entire RBC membrane. On the basis of recent studies, the value of 20% seems more likely, with actin JCs of greater size. It is even possible that the close proximity of the JCs could lead to competition between them and thus force them to reorganise band-3s in favour of one or the other (Lux 2016). Considering 50% to 80% of 1•2 million band-3s, we end up with a density between 4500 and 7000 per μm^2 and thus a value of $_f$ ten to fifteen times greater than that used in (Turlier *et al.* 2016). Finally, the image of the integral protein diffusing in a uniform ocean of lipids, as induced by the Fluid-Mosaic model of Singer and Nicolson, is widely questioned today (Kusumi *et al.* 2005, 2012; Krapf 2015). This induces an additional doubt on the value of the diffusion coefficient $_{s_{B3}}$ since the Saffman-Delbrück relation is based on this older view of the BL.

From all these data, it is difficult to make us a clear idea of the correct value of $_f$. Nevertheless, in order to estimate the sensitivity of the composite models to the value of this parameter, repeating some simulations by multiplying or dividing by ten the value of $_f$ seems reasonable. The results are given in figure 18. They show that there is almost no difference, the evolution curves are almost merged. A very small difference can be observed for the lowest value of $_f$ but it is really very small. This result may certainly seem surprising

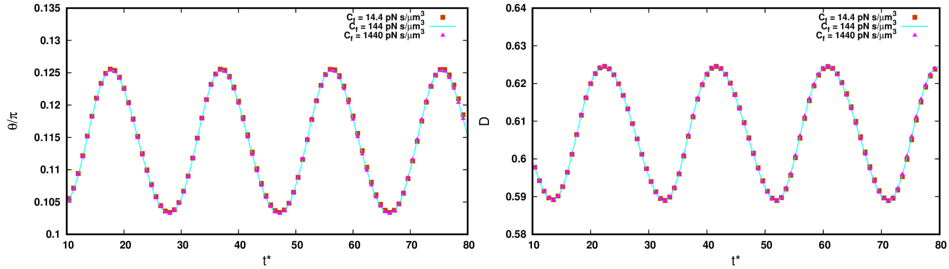

FIGURE 18 – Comparison of inclination angles and deformation on SW/TT dynamics (_ = 0•4- O(W- `) = 0•5) with C-C model for different values of the inter-layer friction coefficient $_f$.

at first sight. However, it should be pointed out that linking to the value of $_f$ the amount of dissipation du to the friction between the SC and the BL is not obvious. Of course, increasing $_f$ at a constant velocity difference would increase the frictional forces. However, the SC is only driven by the BL in its tangential motion through these forces. In other words, increasing the frictional forces leads in turn to a decrease in the velocity difference between the SC and the BL. The conclusion is that the specificity of composite models lies more in the possibility of sliding of the SC relative to the BL than in the intensity of the friction that regulates this sliding. Of course, this conclusion only holds in the framework of our study which forgets all the important relaxation issues related to the consideration of the contribution of surface viscosity.

There is still one point worth discussing. Apart from the stiffening action of the surface incompressibility constraint that our study has highlighted, do the V-C and C-C models differ more fundamentally ? More precisely, the question is about the importance of modelling the BL as a fluid film, in accordance with its material nature. A priori, the fluid nature should allow the BL to adapt more easily to the bulk fluid flow. The surface velocity field of a fluid film may even exhibit vortices if the energy balance is improved. For a BL modelled as a solid shell, such a scenario is of course impossible. To judge the importance of this aspect, we first compare on figures 19 and 20 the surface velocity fields and the streamlines obtained with the C-C and V-C models in SW/TT dynamics. It is difficult to identify a difference in the velocity fields in figure 19, which is typical of the dynamics of TT. On the other hand, a difference in the curvature of the streamlines seems to exist in the figure 20. At C^* = 20, the shapes obtained with the two models are almost identical, making it possible to superimpose the streamlines for comparison. The green lines, obtained with the V-C model, appear more curved than the white ones, obtained with the C-C model. An influence of the mechanical properties of the RBC membrane on the curvature of the current lines in TT dynamics has been anticipated in (Fischer 1992). The curvature of the streamlines was even proposed as an observable to determine the ratio between the surface expansion and shear moduli of the SC, considering that the latter is only entrained by the lipid flow of the BL by friction. The problem addressed in this study was precisely the degree of surface incompressibility imposed on the SC by the BL in TT. The answer depends of course on the ability of the BL to carry the SC along in its movement, which is itself imposed by the ambient fluids. The study concluded that the difference of motion of the SC and BL was very small in TT dynamics, which is confirmed by our study.

The TT dynamics is compatible with a membrane of solid nature. It is also observed for synthetic capsules. Is this the case for all the dynamics adopted by an RBC in a shear flow ? Obviously, the answer is positive for the TU dynamics, which is related to that of a rigid solid body. It is clear that if a counter-example can be found, it is in a regime of very high

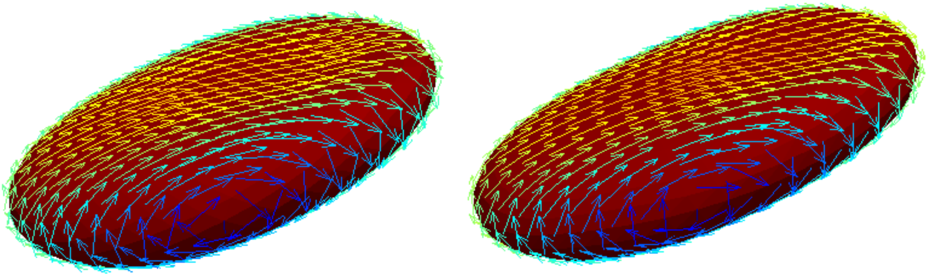

Figure 19 – Comparison of surface velocity fields on SW/TT dynamics (_ = 0•4- O(W- `) = 0•5), with C-C model (left) and V-C model (right), at C* = 33.

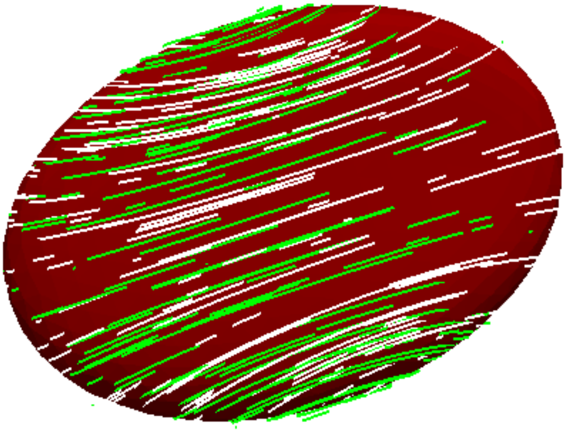

Figure 20 – Comparison of surface streamlines on SW/TT dynamics (_ = 0•4- O(W- `) = 0•5), V-C model (green) versus C-C model (white), at C* = 20.

deformation that it should be sought. For this reason, we have extended our comparison between the C-C and V-C models to the multilobe dynamics. This comparison is illustrated in figure 21. The shapes obtained with the two models when $= {}_{min}$ are comparable. The concavity is slightly less crushed with the V-C model. It is in the shape of the velocity field within this concavity that a more notable difference can be observed. It is well highlighted on the plane projections of the velocity field in this area. The V-C model shows two counter-rotating vortices in the concavity, unlike the C-C model. The widening of the concavity can probably be explained by this phenomenon. Apart from this influence on shape, which remains moderate, it is legitimate to imagine that this difference in surface flow topology may have a more substantial effect on other aspects. The first one that comes to mind is the frictional dissipation between SC and BL that could disturb the energy balance. As we have not considered all the ingredients of this aspect in our models, it is impossible to answer this question. It is not even excluded that considering all potential surface viscosity sources would lead to vortex damping even for the V-C model. The second comes to mind when thinking about the physiological role of a plasma membrane. It is thanks to its fluidity that the proteins it contains can diffuse widely and thus be easily mobilised at certain points to fulfil a biological function. This free diffusion when the RBC is at rest is supplemented by convective transport when the BL is animated by an overall flow.

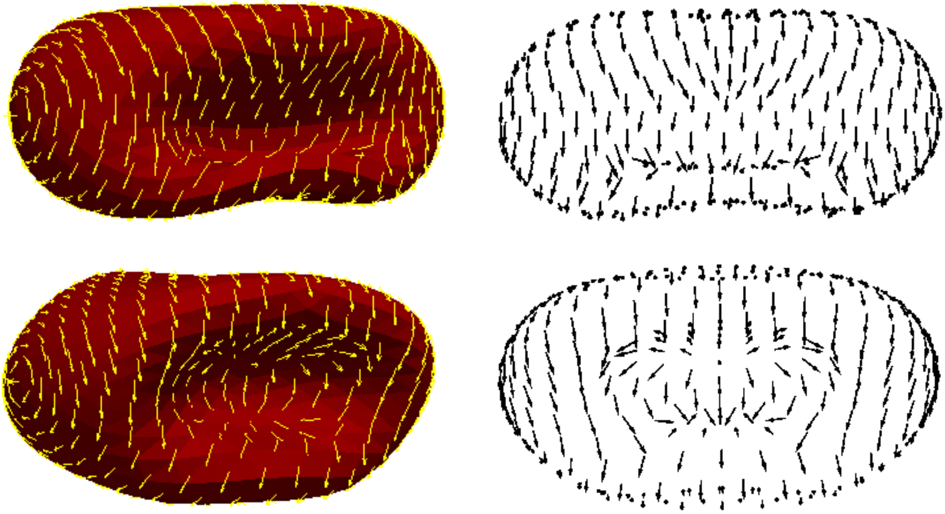

Figure 21 – Comparison of surface velocity fields in the multilobe region (_ = 6•667- 0(W- `) = 1•5), for C-C model (top) and V-C model (bottom), when = $_{min}$. Second column is the zoom of the velocity field in the concavity projected on a plane.

5. Conclusion

Four points (_- 0(W- `)) of the phase diagram are considered in our study. These points were experimentally identified as corresponding to the dynamic regimes of tumbling (TU), tank treading with possible swinging (SW/TT), intermittence in the transition region to tank treading (INT) and finally very high shear leading to multilobe shaped RBCs. While representing all the richness of RBC behaviour in shear flow, the choice of these points allowed us to restrict the study to the case where the RBC symmetry axis remains in the shear plane. Nevertheless, for the SW/TT dynamics, we also considered the alternative where the symmetry axis remains aligned with the vorticity axis. In all cases, the comparison between the modelling strategies is facilitated by the fact that the symmetry axis remains in a plane. Thus, for the analysis of the results, we were able to use the usual indicators which are the inclination angle and the Taylor deformation parameter. Case by case, we supplemented this with other indicators such as the shape of the RBC or the velocity field on its surface.

For all the study points, our results show that modelling the RBC membrane as a single material surface or as two structures that can slide relative to each other is not without consequences. The difference in behaviour between these two modelling strategies may be more or less marked depending on the nature of the dynamics considered, but is always present. It seems difficult to incriminate our particular choices of numerical methods, whether it is a question of spatial and temporal representation or of resolution algorithm. On one hand, our previous studies have demonstrated their accuracy for both vesicle and capsule problems in microflow. More importantly, any criticism that might be made of any of these choices, which is of course always acceptable, would affect all the RBC modelling strategies we have compared. Similarly, the mechanical properties we considered, which are those generally recognised for a healthy RBC, were used equally for all modelling strategies. Only their assignment to one of the modelled component rather than another may vary depending on the strategy adopted. For example, the shear and bending moduli can be assigned to the right structure for a strategy that distinguishes SC from BL. Similarly, the elasticity provided by the SC is necessarily distributed differently when it is represented by a spring network or by a continuous material surface. The only real difference in mechanical properties for the composite BL-SC models comes from the necessity to consider friction between the two layers. This property necessarily induces a surface viscosity phenomenon, not considered in simpler models where the membrane is modelled as a block. However, we have shown in the discussion section that its impact is negligible and that the BL-SC composite models are not very sensitive to the value of the surface friction coefficient which regulates the friction between the SC and the BL.

A first important observation is that representing the SC by a coarse network of springs or by a continuous surface medium is not equivalent. The difference in behaviour relative to a single-layer capsule model (model C) is much more pronounced in the second case. Moreover, the anisotropy artificially induced by the coarseness of the network is detrimental to the numerical stability. It most often leads to model divergence when the BL is represented as a vesicle (V-S model), due to the absence of any other membrane elasticity that can absorb this instability.

A more surprising finding is that the strategy of modelling in one or two layers is more impactful than the choice of the reference shape of the SC, discocyte or quasi-spherical. It is surprising because the question of the reference shape of the SC is a widely debated topic in the community but without considering the type of strategy that is used to produce the numerical results. Certainly, distinguishing the SC from the BL is a much less common strategy than representing the membrane as a single capsule, and is even in the minority. Nevertheless, the body of numerical results available that inform the debate on the reference shape of the SC is derived from both approaches.

Our study does not pretend to identify the best strategy for modelling the RBC membrane. Our intention was just to try to quantify objectively the impact on the numerical results of choosing one strategy over another. Our reasoning was that if this impact is negligible, we might as well favour the least costly strategy, especially for studies of blood rheology. In fact, it was with this prejudice that we set out, with the ambition of demonstrating it. Hence our astonishment at the results which clearly do not allow us to satisfy this initial intention. Overall, the dynamics obtained are in agreement with the experimental observations. It is the key that guided us in the selection of the study points. The observed differences in behaviour remain numerical, without any experimental validation. Moreover, we cannot even anticipate the influence of a more exhaustive integration of all the facets of the mechanics of the RBC, such as the surface viscosity or the passive or active remodelling capacity of the SC. On the other hand, what our study shows is that it is not enough to pay attention to combining all the mechanical properties determining the dynamics of RBC. The way in which they are combined is also important. Due to the lack of experimental comparison, our study does not allow to decide on the best strategy to combine them. Nevertheless, there is an argument that can be put forward. It is that of the fidelity of the model to biological reality while considering the need for numerical efficiency. However, as we pointed out in the section presenting the modelling strategies, the additional cost of a C-C model relative to a C model is low in the context of a continuous material medium description.

A complement to this argument concerns the modelling work. It is of course easier with a strategy that distinguishes the BL from the SC from the start. These two structures are fundamentally different and have completely different physiological functions. To be able to work on each of them separately is certainly a great advantage that allows one to benefit more from the progress made in their experimental investigation and the deeper understanding that follows. Regarding the SC, the models will have to consider its active and passive remodelling capacity. With a composite BL-SC model, this is possible by evolving the surface density of JCs. A satisfactory evolution law has yet to be identified but the possibility is there. Moreover, it is also possible to consider behavioural models more appropriate to polymer networks. The non-linear behaviour model of Soft Glassy Rheology of Sollich *et al.* (1997) has for example been advocated in (Yoon *et al.* 2008). Typically, materials that fall within this model have some degree of structural disorder, combined with the existence of metastable states. At low deformation, the structural elements are frozen in the metastable states and the response is elastic. Beyond that, their energy is sufficient to break through the energy barriers and the material switches to purely viscous dynamics. Concerning the BL, in addition to its fluid nature and its quasi surface incompressibility, other specificities of its organisation seem to influence its mechanical behaviour. The questioning of the Fluid-Mosaic model of Singer and Nicolson has already been mentioned above. The BL is not a lipid ocean in which proteins can diffuse freely. On the one hand, they can be hindered in their movement as soon as the part of them that emerges from the BL on the SC side extends sufficiently to sense the latter. On the other hand, their movement is also influenced by the solid domains that the lipids form more or less temporarily. These domains are the result of a phase separation mechanism that occurs naturally due to the presence of several types of lipids in the BL. Other constituents are also involved, such as cholesterol and sphingomyelin, leading to differently enriched domains. On this last point, the recent experimental study of Leonard *et al.* (2017) has shown that cholesterol-enriched domains are preferentially found in regions of high curvature and sphingomyelin-enriched domains in regions of low curvature. During a deformation, the former gather where the curvature increases. On the contrary, the presence of the latter increases in correspondence with the efflux of 0^{2+} during the phase of restoration of the shape and volume. The study also suggests a relationship between these domains and RBC ageing. Both types of lipid domains were identified as preferred sites of vesiculation. This conclusion could be extended more broadly to pathologic RBCs, the study of which is the other main argument in favour of BL-SC composite modelling strategies. The pathologies may be related to specific defects in each of the two structures, as well as to the protein complexes that link them. For example, the spherocyte shape of RBCs, typical of patients with hereditary spherocytosis, is the result of a defect in ankyrin, 4.2 proteins or band-3 proteins. In contrast, in the pathology of hereditary elliptocytosis, the protein defect rather involves the SC, preventing the self-association of U- and V-spectrin. A review of numerical modelling strategies for the study of pathological RBCs can be found in (Li *et al.* 2017). The importance of distinguishing between SC and BL is stressed.

In adopting this argument, an open question remains. Is the additional cost of modelling the BL as a vesicle rather than a capsule necessary, useful, avoidable ? It should be noted that, to our knowledge, no such model is currently being promoted in the community. Two mechanical properties contributed by the BL are at stake, the surface incompressibility and the fluid nature of the BL. Our results show that the former consistently provides a marked stiffening effect compared to a quasi-incompressible capsule model. It can reduce up to 50% of the breathing phenomenon for the deformation and swinging for the inclination angle in TT dynamics, which is not negligible. The importance of fluidity is less obvious for the case of shear flow and as long as viscous dissipation aspects are not addressed. It is in the very high shear rate regime that the influence becomes noticeable, with even the appearance of contra-rotating vortices impossible to reproduce with a capsule model. Can this have a significant effect on the dynamics of the RBC ? Could it be physiologically important by altering the transport and mobilisation of RBC membrane proteins and receptors ? The question of whether these complex flows within the plasma membrane even exist remains open, although we have shown that considering the fluidity of the BL it is still possible. On the other hand, it is not the consideration of the fluid aspect that is expensive in a vesicle model but the rigorous consideration of the incompressibility constraint by a projection method in a space of surface divergence free velocity field. This remark opens the way to an alternative which should represent a good strategy and which is already widely adopted in the vesicle community. This alternative consists in taking into account the surface incompressibility constraint a little less rigorously but more efficiently in another way, like notably by a penalty method. The degree of satisfaction of the surface incompressibility constraint can be controlled by the penalty coefficient but to a much more satisfactory extent than in a capsule model and while preserving the fluid nature of the BL.

Our motivation in undertaking this study was primarily numerical modelling concerns. However, the results fortuitously raised two points that could take us further in contributing to the biophysical understanding of RBC. The first is the one just mentioned about the role of the fluid nature of the BL but whose importance remains to be verified. The second is the still unresolved question of the reference shape of the SC. Our study in SW/TT dynamics highlights a new phenomenon that could constitute a new indicator. The experimental study of Minetti *et al.* (2019) suggests that in this regime two orientations of the RBC symmetry axis are possible, in the shear plane or aligned with the vorticity axis. For this reason we have considered these two configurations in our study. The conclusion is that with a reference shape close to the sphere for the SC, the steady state dynamics for the two orientations are indistinguishable. Only marker tracking allows us to state that the initial orientation is preserved and that the two dynamics cannot therefore be considered as fully equivalent. With the discocyte reference shape, the result is considerably different and accentuated when moving from the simple capsule model to a composite BL-SC model. With the C model, the amplitude of SW and breathing increases when the symmetry axis is in the shear plane and decreases when aligned with the vorticity axis. Most notable is the halving of the oscillation frequency in the latter case. With the C-C model, the effect is even more radical, since the oscillations disappear completely, giving way to pure TT dynamics. In either case, this influence on the oscillation frequency is perhaps significant enough to be verified experimentally.

Acknowledgements

The project leading to this publication has received funding from France 2030, the French Government program managed by the French National Research Agency (ANR-16-CONV-0001) and from Excellence Initiative of Aix-Marseille University - A*MIDEX. This work was granted access to the HPC resources of Aix-Marseille University.

REFERENCES

Betz, T., Lenz, M., Joanny, J.-F. & Sykes, C. 2009 ATP-dependent mechanics of red blood cells. *Proceedings of the National Academy of Sciences* **106** (36), 15320–15325.

Boedec, G., Leonetti, M. & Jaeger, M. 2017 Isogeometric FEM-BEM simulations of drop, capsule and vesicle dynamics in Stokes flow. *Journal of Computational Physics* **342**, 117–138.

Brochard, F. & Lennon, J.F. 1975 Frequency spectrum of the flicker phenomenon in erythrocytes. *Journal de Physique* **36** (11), 1035–1047.

Bryk, A.H. & Wiśniewski, J.R. 2017 Quantitative Analysis of Human Red Blood Cell Proteome. *Journal of Proteome Research* **16** (8), 2752–2761.

Canham, P.B. 1970 The minimum energy of bending as a possible explanation of the biconcave shape of the human red blood cell. *Journal of Theoretical Biology* **26** (1), 61–81.

Chang, H.-Y., Li, X. & Karniadakis, G.E. 2017 Modeling of Biomechanics and Biorheology of Red Blood Cells in Type 2 Diabetes Mellitus. *Biophysical Journal* **113** (2), 481–490.

Chang, H.-Y., Li, X., Li, He & Karniadakis, G.E. 2016 MD/DPD Multiscale Framework for Predicting Morphology and Stresses of Red Blood Cells in Health and Disease. *PLOS Computational Biology* **12** (10), e1005173.

Chien, S. & Sung, L.A. 1990 Molecular basis of red cell membrane rheology : Part 11. *Biorheology* **27** (3-4), 327–344.

Cirak, F. & Ortiz, M. 2001 Fully C1-conforming subdivision elements for finite deformation thin-shell analysis. *International Journal for Numerical Methods in Engineering* **51** (7), 813–833.

Cirak, F., Ortiz, M. & Schröder, P. 2000 Subdivision surfaces : a new paradigm for thin-shell finite-element analysis. *International Journal for Numerical Methods in Engineering* **47** (12), 2039–2072.

Cottrell, J.A., Hughes, T.J.R. & Bazilevs, Y. 2009 *Isogeometric analysis : toward integration of CAD and FEA*. Chichester, West Sussex, U.K. ; Hoboken, NJ : Wiley, oCLC : ocn335682757.

Dao, M., Li, J. & Suresh, S. 2006 Molecularly based analysis of deformation of spectrin network and human erythrocyte. *Materials Science and Engineering : C* **26** (8), 1232–1244.

Discher, D.E., Boal, D.H. & Boey, S.K. 1998 Simulations of the Erythrocyte Cytoskeleton at Large Deformation. II. Micropipette Aspiration. *Biophysical Journal* **75** (3), 1584–1597.

Dodson, W.R. & Dimitrakopoulos, P. 2010 Tank-Treading of Erythrocytes in Strong Shear Flows via a Nonstiff Cytoskeleton-Based Continuum Computational Modeling. *Biophysical Journal* **99** (9), 2906–2916.

Dupire, J., Socol, M. & Viallat, A. 2012 Full dynamics of a red blood cell in shear flow. *Proceedings of the National Academy of Sciences* **109** (51), 20808–20813.

Evans, E.A. & Hochmuth, R.M. 1978 Mechanochemical Properties of Membranes. In *Current Topics in Membranes and Transport*, , vol. 10, pp. 1–64. Elsevier.

Evans, E.A. & Skalak, R. 2018 *Mechanics and Thermodynamics of Biomembranes*, 1st edn. CRC Press.

Evans, E.A. & Waugh, R. 1977 Osmotic correction to elastic area compressibility measurements on red cell membrane. *Biophysical Journal* **20** (3), 307–313.

Fedosov, D.A., Caswell, B. & Karniadakis, G.E. 2010*a* A Multiscale Red Blood Cell Model with Accurate Mechanics, Rheology, and Dynamics. *Biophysical Journal* **98** (10), 2215–2225.

Fedosov, D.A., Caswell, B. & Karniadakis, G.E. 2010*b* Systematic coarse-graining of spectrin-level red blood cell models. *Computer Methods in Applied Mechanics and Engineering* **199** (29-32), 1937–1948.

Fedosov, D.A., Noguchi, H. & Gompper, G. 2014 Multiscale modeling of blood flow : from single cells to blood rheology. *Biomechanics and Modeling in Mechanobiology* **13** (2), 239–258.

Feng, Z., Waugh, R.E. & Peng, Z. 2020 Constitutive Model of Erythrocyte Membranes with Distributions of Spectrin Orientations and Lengths. *Biophysical Journal* **119** (11), 2190–2204.

Fischer, T.M. 1992 Is the surface area of the red cell membrane skeleton locally conserved ? *Biophysical Journal* **61** (2), 298–305.

Fischer, T.M. 2004 Shape Memory of Human Red Blood Cells. *Biophysical Journal* **86** (5), 3304–3313.

Fischer, T.M., Haest, C.W., Stöhr-Liesen, M., Schmid-Schönbein, H. & Skalak, R. 1981 The stress-free shape of the red blood cell membrane. *Biophysical Journal* **34** (3), 409–422.

Fischer, T.M. & Korzeniewski, R. 2013 Threshold shear stress for the transition between tumbling and tank-treading of red blood cells in shear flow : dependence on the viscosity of the suspending medium. *Journal of Fluid Mechanics* **736**, 351–365.

Freund, J.B. 2014 Numerical Simulation of Flowing Blood Cells. *Annual Review of Fluid Mechanics* **46** (1), 67–95.

Gautier, E.-F., Leduc, M., Cochet, S., Bailly, K., Lacombe, C., Mohandas, N., Guillonneau, F., El Nemer, W. & Mayeux, P. 2018 Absolute proteome quantification of highly purified populations of circulating reticulocytes and mature erythrocytes. *Blood Advances* **2** (20), 2646–2657.

Gounley, J., Boedec, G., Jaeger, M. & Leonetti, M. 2016 Influence of surface viscosity on droplets in shear flow. *Journal of Fluid Mechanics* **791**, 464–494.

Gounley, J. & Peng, Y. 2015 Computational Modeling of Membrane Viscosity of Red Blood Cells. *Communications in Computational Physics* **17** (4), 1073–1087.

Gov, N.S. & Safran, S.A. 2005 Red Blood Cell Membrane Fluctuations and Shape Controlled by ATP-Induced Cytoskeletal Defects. *Biophysical Journal* **88** (3), 1859–1874.

Guglietta, F., Behr, M., Biferale, L., Falcucci, G. & Sbragaglia, M. 2020 On the effects of membrane viscosity on transient red blood cell dynamics. *Soft Matter* **16** (26), 6191–6205, arXiv : 2004.04109.

Hoore, M., Yaya, F., Podgorski, T., Wagner, C., Gompper, G. & Fedosov, D.A. 2018 Effect of spectrin network elasticity on the shapes of erythrocyte doublets. *Soft Matter* **14** (30), 6278–6289.

Hwang, W.C. & Waugh, R.E. 1997 Energy of dissociation of lipid bilayer from the membrane skeleton of red blood cells. *Biophysical Journal* **72** (6), 2669–2678.

Jeffery, G. B. 1922 The motion of ellipsoidal particles immersed in a viscous fluid. *Proceedings of the Royal Society of London. Series A, Containing Papers of a Mathematical and Physical Character* **102** (715), 161–179.

KIM, Y, KIM, K & PARK, Y 2012 Measurement Techniques for Red Blood Cell Deformability : Recent Advances. In *Blood Cell - An Overview of Studies in Hematology* (ed. Terry Moschandreou). InTech.

KRAPF, D. 2015 Mechanisms Underlying Anomalous Diffusion in the Plasma Membrane. In *Current Topics in Membranes*, , vol. 75, pp. 167–207. Elsevier.

KRISHNASWAMY, S. 1996 A cosserat-type model for the red blood cell wall. *International Journal of Engineering Science* **34** (8), 873–899.

KROLL, D. & GOMPPER, G 1992 The conformation of fluid membranes : Monte Carlo simulations. *Science* **255** (5047), 968–971.

KUSUMI, A., FUJIWARA, T.K., CHADDA, R., XIE, M., TSUNOYAMA, T.A., KALAY, Z., KASAI, R.S. & SUZUKI, K.G.N. 2012 Dynamic Organizing Principles of the Plasma Membrane that Regulate Signal Transduction : Commemorating the Fortieth Anniversary of Singer and Nicolson's Fluid-Mosaic Model. *Annual Review of Cell and Developmental Biology* **28** (1), 215–250.

KUSUMI, A., NAKADA, C., RITCHIE, K., MURASE, K., SUZUKI, K., MURAKOSHI, H., KASAI, R.S., KONDO, J. & FUJIWARA, T. 2005 Paradigm Shift of the Plasma Membrane Concept from the Two-Dimensional Continuum Fluid to the Partitioned Fluid : High-Speed Single-Molecule Tracking of Membrane Molecules. *Annual Review of Biophysics and Biomolecular Structure* **34** (1), 351–378.

KÉSMÁRKY, G., KENYERES, P., RÁBAI, M. & TÓTH, K. 2008 Plasma viscosity : A forgotten variable. *Clinical Hemorheology and Microcirculation* **39** (1–4), 243–246, publisher : IOS Press.

LEONARD, C., CONRARD, L., GUTHMANN, M., POLLET, H., CARQUIN, M., VERMYLEN, C., GAILLY, P., VAN DER SMISSEN, P., MINGEOT-LECLERCQ, M. P. & TYTECA, D. 2017 Contribution of plasma membrane lipid domains to red blood cell (re)shaping. *Scientific Reports* **7** (1), 4264.

LEVANT, M. & STEINBERG, V. 2016 Intermediate regime and a phase diagram of red blood cell dynamics in a linear flow. *Physical Review E* **94** (6), 062412.

LI, H., CHANG, H. Y., YANG, J., LU, L., TANG, Y. H. & LYKOTRAFITIS, G. 2018*a* Modeling biomembranes and red blood cells by coarse-grained particle methods. *Applied Mathematics and Mechanics* **39** (1), 3–20.

LI, H. & LYKOTRAFITIS, G. 2012 Two-Component Coarse-Grained Molecular-Dynamics Model for the Human Erythrocyte Membrane. *Biophysical Journal* **102** (1), 75–84.

LI, H. & LYKOTRAFITIS, G. 2014 Erythrocyte Membrane Model with Explicit Description of the Lipid Bilayer and the Spectrin Network. *Biophysical Journal* **107** (3), 642–653.

LI, H. & LYKOTRAFITIS, G. 2015 Vesiculation of healthy and defective red blood cells. *Physical Review E* **92** (1), 012715.

LI, J., DAO, M., LIM, C.T. & SURESH, S. 2005 Spectrin-Level Modeling of the Cytoskeleton and Optical Tweezers Stretching of the Erythrocyte. *Biophysical Journal* **88** (5), 3707–3719.

LI, J., LYKOTRAFITIS, G., DAO, M. & SURESH, S. 2007 Cytoskeletal dynamics of human erythrocyte. *Proceedings of the National Academy of Sciences* **104** (12), 4937–4942.

LI, XUEJIN, LI, HE, CHANG, HUNG-YU, LYKOTRAFITIS, GEORGE & EM KARNIADAKIS, GEORGE 2017 Computational Biomechanics of Human Red Blood Cells in Hematological Disorders. *Journal of Biomechanical Engineering* **139** (2), 021008.

LI, X., LU, H. & PENG, Z. 2018*b* Continuum- and Particle-Based Modeling of Human Red Blood Cells. In *Handbook of Materials Modeling* (ed. W. Andreoni & S. Yip), pp. 1–17. Cham : Springer International Publishing.

LI, X, PENG, Z., LEI, H., DAO, M. & KARNIADAKIS, G.E. 2014 Probing red blood cell mechanics, rheology and dynamics with a two-component multi-scale model. *Philosophical Transactions of the Royal Society A : Mathematical, Physical and Engineering Sciences* **372** (2021), 20130389.

LI, X., VLAHOVSKA, P.M. & KARNIADAKIS, G.E. 2013 Continuum- and particle-based modeling of shapes and dynamics of red blood cells in health and disease. *Soft Matter* **9** (1), 28–37.

LIM, H. W., WORTIS, M. & MUKHOPADHYAY, R. 2002 Stomatocyte-discocyte-echinocyte sequence of the human red blood cell : Evidence for the bilayer- couple hypothesis from membrane mechanics. *Proceedings of the National Academy of Sciences* **99** (26), 16766–16769.

LIU, F., BURGESS, J., MIZUKAMI, H. & OSTAFIN, A. 2003 Sample Preparation and Imaging of Erythrocyte Cytoskeleton with the Atomic Force Microscopy. *Cell Biochemistry and Biophysics* **38** (3), 251–270.

LOOP, C. T. 1987 Smooth Subdivision Surfaces Based on Triangles. Master's thesis, The University of Utah.

LU, H. & PENG, Z. 2019 Boundary integral simulations of a red blood cell squeezing through a submicron slit under prescribed inlet and outlet pressures. *Physics of Fluids* **31** (3), 031902.

LUX, S.E. 2016 Anatomy of the red cell membrane skeleton : unanswered questions. *Blood* **127** (2), 187–199.

LYU, J., CHEN, P.G., BOEDEC, G., LEONETTI, M. & JAEGER, M. 2018 Hybrid continuum–coarse-grained modeling of erythrocytes. *Comptes Rendus Mécanique* **346** (6), 439–448.

LYU, J.M., CHEN, P.G., BOEDEC, G., LEONETTI, M. & JAEGER, M. 2021 An isogeometric boundary element method for soft particles flowing in microfluidic channels. *Computers & Fluids* **214**, 104786.

MAUER, J., MENDEZ, S., LANOTTE, L., NICOUD, F., ABKARIAN, M., GOMPPER, G. & FEDOSOV, D.A. 2018 Flow-Induced Transitions of Red Blood Cell Shapes under Shear. *Physical Review Letters* **121** (11), 118103.

MCWHIRTER, J.L., NOGUCHI, H. & GOMPPER, G. 2011 Deformation and clustering of red blood cells in microcapillary flows. *Soft Matter* **7** (22), 10967.

MENDEZ, S. & ABKARIAN, M. 2018 In-plane elasticity controls the full dynamics of red blood cells in shear flow. *Physical Review Fluids* **3** (10), 101101.

MINETTI, C., AUDEMAR, V., PODGORSKI, T. & COUPIER, G. 2019 Dynamics of a large population of red blood cells under shear flow. *Journal of Fluid Mechanics* **864**, 408–448.

MOHANDAS, N. & EVANS, E. 1994 Mechanical Properties of the Red Cell Membrane in Relation to Molecular Structure and Genetic Defects. *Annual Review of Biophysics and Biomolecular Structure* **23** (1), 787–818.

MOHANDAS, N. & GALLAGHER, P.G. 2008 Red cell membrane : past, present, and future. *Blood* **112** (10), 3939–3948.

NANS, A., MOHANDAS, N. & STOKES, D. 2011 Native Ultrastructure of the Red Cell Cytoskeleton by Cryo-Electron Tomography. *Biophysical Journal* **101** (10), 2341–2350.

NOGUCHI, H. & GOMPPER, G. 2005 Shape transitions of fluid vesicles and red blood cells in capillary flows. *Proceedings of the National Academy of Sciences* **102** (40), 14159–14164.

PAN, L., YAN, R., LI, W. & XU, K. 2018 Super-Resolution Microscopy Reveals the Native Ultrastructure of the Erythrocyte Cytoskeleton. *Cell Reports* **22** (5), 1151–1158.

PENG, Z., ASARO, R.J. & ZHU, Q. 2010 Multiscale simulation of erythrocyte membranes. *Physical Review E* **81** (3), 031904.

PENG, Z., ASARO, R.J. & ZHU, Q. 2011 Multiscale modelling of erythrocytes in Stokes flow. *Journal of Fluid Mechanics* **686**, 299–337.

PENG, Z., CHEN, Y.-L., LU, H., PAN, Z. & CHANG, H.-C. 2015*a* Mesoscale simulations of two model systems in biophysics : from red blood cells to DNAs. *Computational Particle Mechanics* **2** (4), 339–357.

PENG, Z., LI, X., PIVKIN, I. V., DAO, M., KARNIADAKIS, G. E. & SURESH, S. 2013 Lipid bilayer and cytoskeletal interactions in a red blood cell. *Proceedings of the National Academy of Sciences* **110** (33), 13356–13361.

PENG, Z., MASHAYEKH, A. & ZHU, Q. 2014 Erythrocyte responses in low-shear-rate flows : effects of non-biconcave stress-free state in the cytoskeleton. *Journal of Fluid Mechanics* **742**, 96–118.

PENG, Z., SALEHYAR, S. & ZHU, Q. 2015*b* Stability of the tank treading modes of erythrocytes and its dependence on cytoskeleton reference states. *Journal of Fluid Mechanics* **771**, 449–467.

PENG, Z. & ZHU, Q. 2013 Deformation of the erythrocyte cytoskeleton in tank treading motions. *Soft Matter* **9** (31), 7617.

PETERSON, M.A., STREY, H. & SACKMAND@PENI15HG,I-215HZ.I-215H&I-215HZHUI30H,I-215HQ.I TJ@F33@9664T@F7@1.858